

1 **A blended soundproof-to-compressible numerical model for small**
2 **to meso-scale atmospheric dynamics**

3 **TOMMASO BENACCHIO ***, **WARREN P. O'NEILL**, AND **RUPERT KLEIN**

FB Mathematik & Informatik, Freie Universität Berlin, Berlin, Germany

* *Corresponding author address:* Met Office, FitzRoy Road, Exeter EX1 3PB, UK

E-mail: tommaso.benacchio@metoffice.gov.uk

ABSTRACT

4
5 A blended model for atmospheric flow simulations is introduced that enables seamless tran-
6 sition from fully-compressible to pseudo-incompressible dynamics. The model equations are
7 written in non-perturbational form and integrated using a well-balanced second-order finite
8 volume discretization. The semi-implicit scheme combines an explicit predictor for advection
9 with elliptic corrections for the pressure field. Compressibility is implemented in the elliptic
10 equations through a diagonal term. The compressible/pseudo-incompressible transition is
11 realized by suitably weighting the term and provides a mechanism for removing unwanted
12 acoustic imbalances in compressible runs.

13 As the gradient of the pressure is used instead of the Exner pressure in the momentum
14 equation, the influence of perturbation pressure on buoyancy must be included to ensure
15 thermodynamic consistency. With this effect included the thermodynamically consistent
16 model is equivalent to Durran’s original pseudo-incompressible model, which uses the Exner
17 pressure.

18 Numerical experiments demonstrate quadratic convergence and competitive solution qual-
19 ity for several benchmarks. With the inclusion of an additional buoyancy term required
20 for thermodynamic consistency, the “ p - ρ -formulation” of the pseudo-incompressible model
21 closely reproduces the compressible results.

22 The proposed unified approach offers a framework for models that are largely free of
23 the biases which can arise when different discretizations are used. With data assimilation
24 applications in mind, the seamless compressible/pseudo-incompressible transition mechanism
25 is also shown to enable the flattening of acoustic imbalances in initial data for which balanced
26 pressure distributions are unknown.

27 1. Introduction

28 Physical processes in the atmosphere feature a wide range of spatio-temporal scales de-
29 scribed by the fully-compressible non-hydrostatic flow equations. Accordingly, non-hydrostatic
30 fully-compressible modelling approaches hold sway in atmospheric research codes and in op-
31 erational dynamical cores, e.g., ICON (Zängl et al. 2014), NUMA (Kelly and Giraldo 2012),
32 DUNE (Brdar et al. 2013), the models in use at NCAR (Wong et al. 2014), ECMWF (Hortal
33 2002; Smolarkiewicz et al. 2014), the UK Met Office (Davies et al. 2005; Wood et al. 2013),
34 and others.

35 Despite very successful ongoing developments, the proper treatment of multiple charac-
36 teristic time scales in atmospheric simulations remains a matter of scientific research. Two of
37 the biggest obstacles of multiple-scales simulations are (i) the discretization of fast processes
38 in the governing equations and (ii) balanced data assimilation.

39 Numerical stiffness is the source of the first remaining obstacle. Except for inertia-
40 gravity waves of long wavelength, which are not considered here, quantities of meteorological
41 interest propagate at low speed compared with sound waves. Sound modes are said to be
42 nearly balanced and their effects are considered negligible for atmospheric dynamics. The
43 difference between the sound and flow speeds stiffens the numerics of fully-compressible
44 solvers rendering straightforward explicit schemes impractical due to severe stability-related
45 time step constraints.

46 Filtering the data with respect to fast modes while minimally distorting the ensuing
47 dynamics is the second remaining obstacle. Computational simulations never exactly track
48 the evolution of the considered system. Hence, data assimilation is needed for exploiting
49 observational data at regular time intervals to set up initial data for the next simulation pe-
50 riod. However, importing observed field data from local weather stations directly to adjacent
51 grid points would disregard the aforementioned balances of the fast modes. For example,
52 in the presence of a low pressure system in the summer with high levels of convection, the
53 local vertical velocities would project onto non-hydrostatic and compressible modes yielding

54 strongly unbalanced data on the numerical grid. Efficiently controlling such modes remains
55 a challenge in data assimilation.

56 Numerical approaches aimed at overcoming the stiffness are split-explicit, semi-implicit,
57 and fully implicit numerical time integrators for the fully-compressible flow equations. The
58 first class of schemes subcycles a simplified discretization of the fast wave processes at short
59 time steps and employs suitable synchronization procedures for coupling the results to large
60 time steps of the slower modes (Skamarock and Klemp 1994, 2008; Jebens et al. 2009). An-
61 other option would be to adopt a fully implicit approach which even overcomes the time step
62 restrictions associated with explicit discretizations of advection. Due to their computational
63 expense these schemes have, to our knowledge, thus far not found widespread application in
64 meteorology. A notable exception is the work by Reisner et al. (2005).

65 The focus of the present work lies instead on semi-implicit discretizations which invoke
66 implicit integrators for the terms in the equations representing the fast wave modes while
67 treating the slow modes explicitly. Many approaches to semi-implicit discretization for at-
68 mospheric flows have been reported, e.g., by Bonaventura (2000); Gatti-Bono and Colella
69 (2006); Restelli and Giraldo (2009); Jebens et al. (2011); Durran and Blossey (2012); Giraldo
70 et al. (2013); Wood et al. (2013); Smolarkiewicz et al. (2014); Weller and Shahrokhi (2014).
71 For all-speed flow discretizations in computational fluid dynamics the reader is referred to
72 Casulli and Greenspan (1984); Bijl and Wesseling (1998); Munz et al. (2003); Kwatra et al.
73 (2009).

74 An alternative to these numerical approaches to overcoming the stiffness is to adopt a
75 “soundproof” model. These reduced dynamical models include a diagnostic constraint on
76 the velocity divergence and therefore do not support sound waves. The divergence constraint
77 needs to be maintained numerically, which entails the solution of an elliptic pressure equation.
78 Soundproof models suitable for atmospheric motions covering vertical distances comparable
79 to the pressure scale height are the anelastic (Lipps and Hemler 1982; Bannon 1996) and
80 pseudo-incompressible models (Durran 1989; Klein and Pauluis 2011).

81 Soundproof models have successfully been used to simulate small to meso-scale flows, and
82 their validity as slow-flow limit models has recently been established on theoretical grounds
83 (Klein et al. 2010; Achatz et al. 2010). However, their applicability to large-scale motions is
84 still under debate (Davies et al. 2003; Dukowicz 2013) despite recent successful large-scale
85 simulations for atmospheric (Smolarkiewicz and Dörnbrack 2008; Smolarkiewicz et al. 2014)
86 and astrophysical (Nonaka et al. 2010; Smolarkiewicz and Charbonneau 2013) applications.

87 In line with these observations, one of our goals is to develop a numerical scheme for the
88 fully-compressible equations that defaults to the pseudo-incompressible limit for slow flows
89 on small to meso scales. Such asymptotically adaptive schemes have a substantial history of
90 studies (Klein 2000; Klein et al. 2001; Gatti-Bono and Colella 2006; Cullen 2007; Haack et al.
91 2012) in which the low Mach or low Froude number limits are discretely recovered through
92 careful identification and separate discretization of the advection, acoustic, and/or buoyancy
93 terms in the fully-compressible equations. In the present work we suggest a particularly
94 straightforward approach of this type that is directly motivated by the theoretical framework
95 set out in Klein (2009, 2010).

96 More specifically, this paper documents the construction of a semi-implicit second-order
97 accurate numerical method for the simulation of weakly compressible atmospheric flows that
98 shares the principal components of the discretization with the soundproof solver by Klein
99 (2009). The time integration for the fully compressible equations derives from that of the
100 pseudo-incompressible model and the required adjustments amount to no more than adding
101 a diagonal term to the matrix of the elliptic pressure problem and synchronizing the cell-
102 centered and node-based pressures. This is similar in spirit to parallel developments by
103 Smolarkiewicz et al. (2014) but technically different. In particular, these authors do not
104 address the possibility of a seamless blending of models and they work with perturbation
105 variables and with the Exner pressure in the momentum equation.

106 Besides constructing the compressible flow solver, we design the discretization such that
107 it can be used directly to solve a continuous family of weakly compressible models that

108 interpolate seamlessly between the fully-compressible and pseudo-incompressible ones. This
109 is realized by exploiting the close structural similarity of these two limiting models when
110 written in conservative, non-perturbational form for the densities of mass, momentum, and
111 potential temperature.

112 In the context of increasing computing resources and ever smaller scales accessible in
113 high-resolution weather and climate simulations, it is of arguable interest to operate differ-
114 ent analytical formulations within a single numerical framework. Such a unified numerical
115 scheme becomes all the more desirable in the light of a recent study (Smolarkiewicz and
116 Dörnbrack 2008) that compared the errors made by using different numerical methods for
117 the same model equations with those made by considering different equation systems dis-
118 cretized with nearly identical numerics. These authors found, somewhat surprisingly, that
119 the former errors exceeded the latter, and this underlines the importance of comparing flow
120 models within one and the same numerical framework. In an interesting investigation of this
121 type, Smith and Bannon (2008) compared anelastic and compressible models in a case of
122 localized instantaneous diabatic warming.

123 A second motivation for implementing the seamless model family lies in its potential use
124 for balanced data assimilation. By adjusting the model interpolation parameter accordingly
125 from zero to unity, such a “blended” scheme can be tuned to perform a few time steps
126 in pseudo-incompressible mode and to then transition to its fully-compressible mode after
127 a few further steps. As we will show, this effectively reduces initial acoustic imbalances.
128 Considering the factors affecting predictability of the simulated precipitation field in cloud-
129 resolving models, Hohenegger and Schär (2007) showed that uncontrolled small-scale acoustic
130 perturbations may contribute to rapid error growth at the mesoscale.

131 The scheme we propose has more potentially attractive features. One of these features
132 is the formulation in a non-perturbational form that does not rely on subtraction of a back-
133 ground state for accuracy. This is achieved for the present collocated finite volume method
134 by a well-balanced discretization of the pressure gradient and gravity terms following Botta

135 et al. (2004); Klein (2009). Moreover, the scheme uses the gradient of the thermodynamic
 136 instead of the Exner pressure, thereby allowing for a conservative discretization of the mo-
 137 mentum flux induced by the pressure force. In addition, as pointed out by Klein and Pauluis
 138 (2011), Durran’s original formulation of the pseudo-incompressible model using Exner pres-
 139 sure cannot be easily extended to general equations of state. One step towards overcoming
 140 this obstacle is to adopt a formulation with pressure instead of Exner pressure in the momen-
 141 tum equation as done in this paper. Yet, this formulation is thermodynamically consistent
 142 only if first-order density perturbations are included in the gravity term in addition to Dur-
 143 ran’s “pseudo-density”. For an ideal gas with constant specific heat capacities, Durran’s
 144 model and the present thermodynamically consistent formulation are equivalent as a short
 145 calculation using the transformations $\pi_0 = (p_0/p_{\text{ref}})^{R/c_p}$ and $\pi' = p'/(c_p P_0)$ shows. A second
 146 step that is also necessary in extending to general equations of state, but which is not pursued
 147 here, is a reformulation of the velocity divergence constraint. This step is needed because in
 148 this case the pressure equation can no longer be easily cast into a simple conservation law
 149 (Almgren et al. 2006a,b; Klein and Pauluis 2011).

150 Furthermore, the transition from the pseudo-incompressible via the blending to the com-
 151 pressible model is achieved by minimal code adjustments. These involve reassigning certain
 152 weights in the grid stencil of the elliptic correction equations and applying a weighted super-
 153 position of pressure updates. These updates are calculated from the elliptic equations and
 154 from the conservative balance of potential temperature.

155 The paper is structured as follows. Compressible, pseudo-incompressible, and blended
 156 models are presented in section 2. Section 3 summarizes the numerics. The results of
 157 numerical simulations in a number of two-dimensional test cases is documented in section 4.
 158 Grid convergence with the expected second-order rate is verified in a benchmark involving
 159 advection of a smooth axisymmetric vortex. For the standard test cases of a rising hot
 160 air thermal, density current and inertia-gravity waves, we compare the predictions obtained
 161 with the compressible and pseudo-incompressible models and demonstrate the importance

162 of the thermodynamic consistency correction within the pseudo-incompressible framework.
 163 Usage of the blended model for filtering acoustic imbalances is demonstrated for both short
 164 sound-resolving time steps and for time steps corresponding to an advective CFL number
 165 of order unity. Section 5 provides a concluding discussion and an outline of open issues and
 166 future work.

167 2. Theoretical Framework

168 *Fully-compressible equations*

169 The dry, inviscid fully-compressible equations, henceforth referred to as “FC”, describe
 170 conservation of mass, momentum, and energy under the influence of gravity. If we neglect
 171 rotational effects and use the transport equation for potential temperature to describe the
 172 energy balance, they read in conservative form and in the dry adiabatic case,

$$\frac{\partial \rho}{\partial t} + \nabla \cdot (\rho \mathbf{v}) = 0, \quad (1a)$$

$$\frac{\partial \rho \mathbf{v}}{\partial t} + \nabla \cdot (\rho \mathbf{v} \circ \mathbf{v} + p \mathbf{I}) = -\rho g \mathbf{k}, \quad (1b)$$

$$\frac{\partial P}{\partial t} + \nabla \cdot (P \mathbf{v}) = 0. \quad (1c)$$

173 Here, ρ denotes the fluid density, \mathbf{v} the velocity vector, \circ the tensor product, g the acceler-
 174 ation of gravity, \mathbf{k} the vertical unit vector, and \mathbf{I} the identity tensor. As in Klein (2009), we
 175 have introduced the equation of state

$$P = \rho \theta = \frac{p_{\text{ref}}}{R} \left(\frac{p}{p_{\text{ref}}} \right)^{\frac{1}{\gamma}}, \quad (2)$$

176 where potential temperature is defined as

$$\theta = T \left(\frac{p}{p_{\text{ref}}} \right)^{\frac{1-\gamma}{\gamma}} \quad \text{and} \quad T = \frac{p}{\rho R} \quad (3)$$

177 is the temperature. R is the gas constant for dry air, γ is the isentropic exponent, respectively.
 178 Hereafter, we take $\gamma = 1.4$ and $R = 287 \text{ N m kg}^{-1} \text{ K}^{-1}$ throughout. For smooth flows,

179 (1c) can equivalently replace total energy conservation in a finite volume discretization,
 180 which is common in numerical meteorology, but which would not be adequate for flows
 181 with shocks (LeVeque 2002). Together, (1a) and (1c) describe mass conservation and the
 182 advection of potential temperature, while (1c) is equivalent to the pressure evolution equation
 183 $p_t + \mathbf{v} \cdot \nabla p + \gamma p \nabla \cdot \mathbf{v} = 0$. Thus, a discretization of (1c) directly controls the pressure evolution,
 184 and this is central to the blended compressible–soundproof formulation to be presented below.

185 The system is closed by appropriate initial and boundary conditions which we will specify
 186 in conjunction with specific test cases below.

187 For later reference, using (2), we compute

$$\frac{\partial P}{\partial p} = \frac{1}{R\gamma} \left(\frac{p}{p_{\text{ref}}} \right)^{\frac{1}{\gamma}-1} = \frac{1}{R\gamma} \left(\frac{PR}{p_{\text{ref}}} \right)^{1-\gamma}. \quad (4)$$

188 *The pseudo-incompressible approximation*

189 The pseudo-incompressible model (Durrán 1989) is commonly derived from a compress-
 190 ible model that formulates the pressure gradient term in the momentum equation using the
 191 Exner pressure,

$$\pi = \left(\frac{p}{p_{\text{ref}}} \right)^{\frac{\gamma-1}{\gamma}} \quad (5)$$

192 so that, in view of (3), one finds

$$\frac{1}{\rho} \nabla p \equiv c_p \theta \nabla \pi. \quad (6)$$

193 To retain flexibility of the developed code, in particular with respect to generalizations of
 194 the equation of state, we adopt the p – ρ formulation here (Klein and Pauluis 2011). When
 195 written in the latter form, extra care must be taken in formulating the momentum equation
 196 to ensure that it retains the influences of the pressure perturbation up to first order.

197 As in Durrán (1989) we start our derivations by assuming that the pressure does not
 198 vary much from its hydrostatic background value and can be written as

$$p = p_0(z) + p'(\mathbf{x}, t), \quad (7)$$

199 where $p'/p_0 \ll 1$ and

$$\frac{\partial p_0}{\partial z} = -\rho_0 g. \quad (8)$$

200 Using (7) in the equation of state (2) gives, with a Taylor expansion,

$$\rho = \frac{1}{\theta} \frac{p_{ref}}{R} \left(\frac{p_0 + p'}{p_{ref}} \right)^{1/\gamma} \approx \frac{1}{\theta} \frac{p_{ref}}{R} \left(\frac{p_0}{p_{ref}} \right)^{1/\gamma} \left(1 + \frac{p'}{\gamma p_0} \right) = \rho^* \left(1 + \frac{p'}{\gamma p_0} \right) \quad (9)$$

201 where ρ^* is called the ‘‘pseudo-density’’ and is defined as the density calculated at the
202 background pressure but using the full potential temperature, i.e.

$$\rho^* = \frac{1}{\theta} \frac{p_{ref}}{R} \left(\frac{p_0}{p_{ref}} \right)^{1/\gamma} = \rho(p_0, \theta). \quad (10)$$

203 To filter sound waves we suppress the effect of pressure perturbations on density to obtain

$$(\rho^*)_t + \nabla \cdot (\rho^* \mathbf{v}) = 0. \quad (11)$$

204 However, in the momentum equation we want to keep the effect of the pressure perturbations
205 up to first order. Using an expansion as in (10) we re-write (1b) in non-conservative form

$$\mathbf{v}_t + \mathbf{v} \cdot \nabla \mathbf{v} + \frac{1}{\rho^*} \left(1 - \frac{p'}{\gamma p_0} \right) \nabla (p_0 + p') = -g \mathbf{k}. \quad (12)$$

206 Keeping terms in (12) up to first order in the pressure perturbation and re-arranging we get

$$\mathbf{v}_t + \mathbf{v} \cdot \nabla \mathbf{v} + \frac{1}{\rho^*} \nabla (p_0 + p') = - \left(1 + \frac{1}{\rho^*} \frac{\rho_0}{\gamma p_0} p' \right) g \mathbf{k}. \quad (13)$$

207 We re-write (13) in conservative form by multiplying by ρ^* and using (11),

$$(\rho^* \mathbf{v})_t + \nabla \cdot (\rho^* \mathbf{v} \circ \mathbf{v}) + \nabla p = - \left(\rho^* + \frac{\rho_0}{\gamma p_0} p' \right) g \mathbf{k}. \quad (14)$$

208 Lastly, we redefine P as

$$P \approx \rho^* \theta = \frac{p_{ref}}{R} \left(\frac{p_0}{p_{ref}} \right)^{1/\gamma} = P_0 \quad (15)$$

209 and (1c) becomes

$$(P_0)_t + \nabla \cdot (P_0 \mathbf{v}) = \nabla \cdot (P_0 \mathbf{v}) = 0. \quad (16)$$

210 In (16) we have used that P is now a function of p_0 only which allows us to drop the time
 211 derivative term and the evolution equation becomes a divergence constraint. This constraint
 212 enforces the pseudo-incompressible form of the density equation in (11) thereby filtering the
 213 effect of pressure perturbations on the density and thus filtering sound waves.

214 The complete pseudo-incompressible governing equations are given by

$$(\rho^*)_t + \nabla \cdot (\rho^* \mathbf{v}) = 0 \quad (17a)$$

$$(\rho^* \mathbf{v})_t + \nabla \cdot (\rho^* \mathbf{v} \circ \mathbf{v}) + \nabla p = - \left(\rho^* + \frac{\rho_0}{\gamma p_0} p' \right) g \mathbf{k} \quad (17b)$$

$$\nabla \cdot (P_0 \mathbf{v}) = 0 \quad (17c)$$

215 Klein (2009) showed agreement between (17a)-(17c) and the original formulation of Dur-
 216 ran (1989) to leading and first order in a perturbation expansion for small pressure varia-
 217 tions. Moreover, if Exner pressure variables are introduced so that $\pi_0 = (p_0/p_{\text{ref}})^{R/c_p}$ and
 218 $\pi' = p'/(c_p P_0)$, a straightforward calculation shows that the original formulation of Durran
 219 (1989) and the present $\text{PI}_{\rho,p}^{\text{tc}}$ formulation are actually *equivalent* at the level of the partial
 220 differential equations. An advantage of our formulation is that it is more easily extended to
 221 incorporate more complex equations of state and that it is “thermodynamically consistent”.
 222 This notion refers to the existence of well-defined thermodynamic potentials describing the
 223 proper increase/decrease of an entropy variable in the diabatic case (Klein and Pauluis 2011).
 224 Note, however, that completing the extension to general equations of state also requires a
 225 reformulation of the divergence constraint (Almgren et al. 2006a,b; Klein and Pauluis 2011).

226 *A blended compressible/pseudo-incompressible model*

227 In Klein (2009) the task of incorporating the time derivative term in (1c) and modelling
 228 the fully-compressible dynamics was left for future work. Here we aim to merge the com-
 229 pressible, pseudo-incompressible, and thermodynamically consistent discretizations in the
 230 “ p - ρ -formulation” for the momentum equation in a single numerical model featuring

- 231 • a conservative discretization with respect to $\rho, \rho\mathbf{v}, \rho\theta \equiv P$,
- 232 • second-order accuracy,
- 233 • time steps independent of the sound speed,
- 234 • a continuous transition between pseudo-incompressible and compressible forms,
- 235 • a well-balanced discretization that does not rely on subtraction of a background state.

236 The blended equations are given as follows, for $\alpha \in \{0, 1\}$:

$$\rho_t + \nabla \cdot (\rho\mathbf{v}) = 0, \quad (18a)$$

$$(\rho\mathbf{v})_t + \nabla \cdot (\rho\mathbf{v} \circ \mathbf{v}) + \nabla p = -g\mathbf{k} \left(\rho + (1 - \alpha) \beta \frac{\rho_0}{\gamma p_0} p' \right), \quad (18b)$$

$$\alpha P_t + \nabla \cdot (P\mathbf{v}) = 0. \quad (18c)$$

237 For $\alpha = 0$ the two pseudo-incompressible models with the “ p - ρ -formulation” of the pressure
 238 gradient term are retrieved. Then, setting $\beta = 1$ selects the thermodynamically consistent
 239 ($\text{PI}_{\rho,p}^{\text{tc}}$) model whereas setting $\beta = 0$ retrieves the “naive” pseudo-incompressible ($\text{PI}_{\rho,p}$)
 240 model. We note that in $\text{PI}_{\rho,p}$ and $\text{PI}_{\rho,p}^{\text{tc}}$ the density ρ takes the role of the pseudo-density,
 241 which was denoted by ρ^* in (17b), and necessitates the additional term for thermodynamic
 242 consistency in the momentum equation (18b) for $(\alpha, \beta) = (0, 1)$. As the model parameter
 243 α is adjusted from 0 to 1, the effect of pressure perturbations on density is retrieved in
 244 a continuous fashion. This formulation recovers the fully-compressible (FC) dynamics for
 245 $\alpha = 1$. A summary of the model configurations is given in Table 1.

246 System (18) features unapproximated mass and momentum equations for $\alpha \in \{0, 1\}$
 247 when $\beta = 1$. The reason is that the $\text{PI}_{\rho,p}^{\text{tc}}$ model is equivalent to Durran’s original pseudo-
 248 incompressible model with the “ π - θ -formulation” of the pressure gradient term. Klein et al.
 249 (2013) observe that the model satisfies an energy conservation law with a definition of the
 250 total energy that is an interpolation between those of the fully-compressible and the pseudo-
 251 incompressible models. The model’s internal wave dispersion properties for realistic stratifi-
 252 cations are close to those of the limiting models. This follows from related analyses for the

253 limiting models by Klein (2010) and the fact that the underlying Sturm-Liouville problems
254 depend smoothly on the defining data. We also refer to Vasil et al. (2013) for related analysis
255 and relegate further discussion to a future publication.

256 In (18) the α and β parameters are introduced to formulate the FC, $\text{PI}_{\rho,p}^{\text{tc}}$, and $\text{PI}_{\rho,p}$
257 models conveniently in one and the same set of equations. Only discrete values $\alpha, \beta \in \{0, 1\}$
258 make sense to begin with. Yet, let us consider the resulting model equations for any $\alpha \in [0, 1]$.
259 A seamless discretization that allows integration of (18) for any of these values can be used
260 to our advantage in some meteorologically interesting situation.

261 Suppose we are to initialize one of the well-known test cases of a rising warm-air bubble
262 or flow over a mountain. As in “real meteorology”, we are not interested in acoustic pertur-
263 bations and would like to simulate acoustically balanced flows. Yet, we have no analytical
264 way to determine the balanced pressure distributions that would be associated with given
265 initial data for potential temperature and velocity.

266 However, knowing that the pseudo-incompressible models provide good approximations
267 to compressible flows free of sound waves, we can attempt to generate reasonable approxi-
268 mations to the missing pressure fields by starting a simulation pseudo-incompressibly with
269 $\alpha = 0$ for, say, S_1 time steps. Within the next S_2 time steps we increase α continuously
270 from 0 to 1, and after time step $S_1 + S_2$ we maintain $\alpha = 1$ to operate the model in fully-
271 compressible mode. This procedure should generate a compressible flow simulation that is
272 balanced with respect to acoustic modes essentially from the start. Promising related results
273 for the rising bubble test are discussed in section 4 below.

274 We conjecture that such a smooth blending of balanced and unbalanced model equations
275 within a common discretization framework could substantially contribute to resolving similar
276 balancing issues in the context of data assimilation.

277 3. Numerical Framework

278 A semi-implicit finite volume method is used to approximate the dynamics of the blended
 279 model. The scheme is a variant and extension of the soundproof solver described in Klein
 280 (2009). An outline is presented here, for more details see Appendix. The discrete solution
 281 of (18) is obtained by the following time stepping procedure, say from t^n to t^{n+1} :

- 282 • An explicit predictor solves an auxiliary hyperbolic system obtained by replacing the
 283 pressure gradient in the momentum equation (18b) with its value at time level t^n . This
 284 step yields second-order accurate ρ , θ and P ;
- 285 • A first elliptic corrector solves for the cell-centered pressure time increment $\delta p =$
 286 $p^{n+1} - p^n$ by enforcing consistency with the pressure equation (18c). This step also
 287 corrects the advecting fluxes in (18a) and (18b);
- 288 • The solution of a second elliptic problem is used to correct the pressure-related mo-
 289 mentum flux for fully second-order accurate updates of the cell-centered momenta.

290 For the time discretization we divide the simulation time interval $[0, T]$ into N subinter-
 291 vals, with $t_0 = 0$, $t^{n+1} = t^n + (\Delta t)^n$ for $n = 0, 1, \dots, N - 1$. For any variable X , we denote
 292 $X^n = X(t^n)$. $(\Delta t)^n = O(T/N)$ denote the time steps. In the implementation, a dynamically
 293 adaptive choice of the time step based on fixing the Courant number is implemented, see
 294 Appendix for details. The spatial domain is divided into primary computational cells $C_{i,j}$
 295 (finite volumes) with $i = 1, \dots, \mathcal{N}_x$, $j = 1, \dots, \mathcal{N}_z$, in two dimensions according to a carte-
 296 sian grid arrangement. The cells $C_{i,j}$ are separated by interfaces $I_{i+1/2,j}, I_{i,j+1/2}$ as shown in
 297 Fig. 1. The extension to three dimensions is straightforward. The primary variables $\rho, \rho \mathbf{v}, P$
 298 are stored at the centers of the primary cells $C_{i,j}$. Pressures are computed at centers of the
 299 primary cells $C_{i,j}$ in the first correction step and at the centers of the dual cells $\bar{C}_{i+1/2,j+1/2}$
 300 shown in Fig. 1 in the second correction step.

301 *Step 1: Predictor*

302 In the first sub-step for a full time step $t^n \rightarrow t^{n+1}$, the following auxiliary hyperbolic
 303 system, obtained from (18) by freezing p and p' at time level t^n , is solved (Klein 2009):

$$\frac{\partial \rho}{\partial t} + \nabla \cdot (\rho \mathbf{v}) = 0, \quad (19a)$$

$$\frac{\partial \rho \mathbf{v}}{\partial t} + \nabla \cdot (\rho \mathbf{v} \circ \mathbf{v} + p^n \mathbf{I}) = -g \mathbf{k} \left(\rho + (1 - \alpha) \beta \frac{\rho_0}{\gamma p_0} (p')^n \right), \quad (19b)$$

$$\frac{\partial P}{\partial t} + \nabla \cdot (P \mathbf{v}) = 0. \quad (19c)$$

304 A two-stage strong stability-preserving Runge-Kutta method (Gottlieb et al. 2001) is used for
 305 time integration here (Klein (2009) instead used a MUSCL technique and directional operator
 306 splitting). The spatial discretization at any stage of the Runge-Kutta time integrator is
 307 performed with a finite volume approach. That is, discrete variables X_C , $X = \rho$, $\rho \mathbf{v}$, P , are
 308 defined as approximations of the cell averages set at the cell centers:

$$X_C = \frac{1}{|C|} \int_C X dx + O(\Delta x^2), \quad (20)$$

309 where $|C|$ is the cell volume. To achieve second-order accuracy in space, piecewise linear
 310 reconstruction of P , \mathbf{v} , and the advected quantities $(1/\theta, \mathbf{v}/\theta)$ is applied within the grid cells.
 311 The reconstructed values are used to determine any data required at grid cell interfaces and
 312 to evaluate the numerical flux functions. The pressure variables $p^n, (p')^n$ are set at the grid
 313 nodes.

314 New values of X_C are obtained from the old ones subtracting the net outflow fluxes at
 315 the boundaries and adding the contributions from the source terms:

$$\rho_C^{n+1,*} = \rho_C^n - \Delta t \left(\tilde{\nabla} \cdot (P \mathbf{v} \theta^{-1}) \right)_C^{n+\frac{1}{2},*}, \quad (21a)$$

$$(\rho \mathbf{v})_C^{n+1,*} = (\rho \mathbf{v})_C^n - \Delta t \left(\tilde{\nabla} \cdot (P \mathbf{v} \circ \mathbf{v} \theta^{-1} + p^n \mathbf{I}) \right)_C^{n+\frac{1}{2},*} - \Delta t g \mathbf{k} (P/\theta + (\rho')^n)_C^{n+\frac{1}{2},*}, \quad (21b)$$

$$P_C^{n+1,*} = P_C^n - \Delta t \left(\tilde{\nabla} \cdot (P \mathbf{v}) \right)_C^{n+\frac{1}{2},*}, \quad (21c)$$

316 where $\rho' = (1 - \alpha) \beta (\rho_0 / \gamma p_0) p'$. The superscripts $(\cdot)^{n+1/2,*}$ in (21) indicate effective time

317 averaged terms as they emerge from the chosen time integrator, and the asterisk indicates
 318 quantities evaluated in the course of the predictor step.

319 Note, we have rewritten the ρg term in the momentum equation (21b) in terms of P and
 320 θ using the equation of state (given by (2) for the FC model and (15) for the $\text{PI}_{\rho,p}$ and $\text{PI}_{\rho,p}^{\text{tc}}$
 321 models) where in the pseudo-incompressible cases $P^{n+\frac{1}{2},*} \equiv P_0$. In the compressible case, in
 322 agreement with second order accuracy we use $P^{n+\frac{1}{2},*} = P^n + \frac{1}{2}\delta p (\partial P/\partial p)$, where δp here
 323 is the pressure increment computed in the correction step of the previous time loop. The
 324 derivative of P with respect to p is computed using the equation of state.

325 By writing ρg in this way we were able to decouple the buoyancy term from the small
 326 advective flux divergence errors that arise in the predictor step. Potential temperature effects
 327 can fully be accounted for in the predictor, because potential temperature is accurately
 328 advected and not affected by the divergence errors. However, the pressure does react to
 329 divergence errors. By relying on accurate pressure information computed during the previous
 330 time steps, the buoyancy term is shielded from this effect. As a result, this formulation was
 331 found to give models increased stability for larger time steps.

332 We have used the following symbolic notation to abbreviate the balance of a numerical
 333 flux, say \mathbf{q} , across grid cell boundaries,

$$\tilde{\nabla} \cdot \mathbf{q}_C = \frac{1}{|C|} \sum_{I \in \mathcal{I}_C} \mathbf{q}_I \cdot \mathbf{n} = \frac{1}{|C|} \oint_{\partial C} \mathbf{q} \cdot \mathbf{n} dl + O(\Delta x^2). \quad (22)$$

334 Here ∂C is the boundary of cell C . See Appendix for further details on the numerical scheme
 335 used in the predictor.

336 Note that we discretize advection by considering $P\mathbf{v}$ as the carrier flux that transports
 337 (upwind) values of the advected quantities $(1/\theta, \mathbf{v}/\theta, 1)$. This has turned out to be advanta-
 338 geous in many respects, e.g., in the construction of a positivity preserving advection scheme
 339 in Klein (2009) (see also Smolarkiewicz et al. (2014) and references therein).

340 We consciously refrain from going into more detail here because many different combina-
 341 tions of second-order accurate finite volume space discretizations and time integrators can
 342 more or less interchangeably be employed for the predictor step, provided they are used in

343 conjunction with a well-balanced discretization of the pressure-gradient and gravity terms,
 344 see, e.g., Botta et al. (2004); Klein (2009). The details of the scheme used to generate the
 345 results of section 4 are given in the Appendix.

346 At the end of the predictor step,

- 347 • the scalar variables ρ , θ and P are second-order accurate (Klein 2009),
- 348 • the advecting fluxes $(P\mathbf{v})^{n+1/2}$ do not comply with the divergence constraint for $\alpha = 0$,
 349 and they do not provide a *stable* update of P for $\alpha > 0$, and
- 350 • using the old time level pressure in the momentum equation (21b) prevents the scheme
 351 from being fully second-order accurate.

352 Crucially, for all values of α the time step used is limited by a CFL stability condition
 353 (Courant et al. 1928) independent of sound speed (see Appendix), so that we sidestep the
 354 stiffness induced by sound waves.

355 *Step 2: First Correction*

356 The first correction step, which is the first of two linearly implicit substeps, corresponds
 357 to the MAC-projection in projection methods for incompressible flows (Bell et al. 1991). The
 358 advecting fluxes $P\mathbf{v}$ used in the predictor step do not abide by a semi-implicit discretization
 359 of the P equation for the FC model and by the divergence constraint for the $\text{PI}_{\rho,p}$ and
 360 $\text{PI}_{\rho,p}^{\text{tc}}$ models. In the first correction, an elliptic equation for a cell-centered pressure update
 361 $\delta p = p^{n+1} - p^n$ is derived by approximating (18c) at the half time level $t^{n+1/2}$, i.e., by
 362 reconsidering

$$\left[\alpha \left(\frac{\partial P}{\partial t} \right) + \nabla \cdot (P\mathbf{v}) \right]^{n+\frac{1}{2}} = 0. \quad (23)$$

363 The predictor step is discretized with second-order accuracy in time. As a consequence, the
 364 advecting fluxes $(P\mathbf{v})^{n+1/2,*}$ already include a first-order accurate update to the half time

365 level according to the auxiliary equation system (19), and this is sufficient to maintain second-
 366 order accuracy for advection. Yet, for stability reasons an implicit correction is added that
 367 accounts for the influence of the new time level pressure gradient in the momentum equation
 368 in the following form (Klein 2009):

$$(P\mathbf{v})^{n+\frac{1}{2}} = (P\mathbf{v})^{n+\frac{1}{2},*} - \frac{\Delta t}{2}\theta^{n+\frac{1}{2},*}\nabla\delta p. \quad (24)$$

369 Again, the asterisk denotes predicted values. Since $\Delta t \delta p = \Delta t (p^{n+1} - p^n) = O((\Delta t)^2)$,
 370 this correction does not affect the second-order accuracy of advection. For $\alpha \neq 0$, the time
 371 derivative term is transformed as:

$$\left(\frac{\partial P}{\partial t}\right)^{n+1/2} = \left(\frac{\partial P}{\partial p} \frac{\partial p}{\partial t}\right)^{n+1/2} = \left(\frac{\partial P}{\partial p}\right)^{n+1/2,*} \frac{\delta p}{\Delta t} + O((\Delta t)^2). \quad (25)$$

372 Using (24) and (25) in (23) we obtain the elliptic problem for any $\alpha \in [0, 1]$,

$$-\alpha \left(\frac{\mathcal{C}_H^{n+\frac{1}{2},*}}{\Delta t} \delta p\right)_C + \tilde{\nabla} \cdot \left(\frac{\Delta t}{2} \theta^{n+\frac{1}{2},*} \nabla \delta p\right)_C = \tilde{\nabla} \cdot \left((P\mathbf{v})^{n+\frac{1}{2},*}\right)_C, \quad (26)$$

373 where

$$\mathcal{C}_H^{n+1/2,*} = \left(\frac{\partial P}{\partial p}\right)^{n+1/2,*}. \quad (27)$$

374 Expression (26) is responsible for determining stable time increments of P in the compressible
 375 model ($\alpha = 1$), whereas it enforces the divergence constraint for $\alpha = 0$.

376 With the solution of (26) δp at hand, the advecting flux corrections read

$$\delta P\mathbf{v} \cdot \mathbf{n} = -\frac{\Delta t}{2}\theta\nabla\delta p \cdot \mathbf{n}, \quad (28)$$

377 and the predicted values are corrected by,

$$\begin{aligned} \rho_C^{n+1} &= \rho_C^{n+1,*} - \Delta t \tilde{\nabla} \cdot (\delta P\mathbf{v} \theta^{-1})_C, \\ (\rho\mathbf{v})_C^{n+1,**} &= (\rho\mathbf{v})_C^{n+1,*} - \Delta t \tilde{\nabla} \cdot (\delta P\mathbf{v} \circ \mathbf{v}\theta^{-1})_C, \\ P_C^{n+1} &= P_C^{n+1,*} - \Delta t \tilde{\nabla} \cdot (\delta P\mathbf{v})_C. \end{aligned} \quad (29)$$

378 where the advected variables θ^{-1} and $\mathbf{v}\theta^{-1}$ are evaluated at $(\cdot)^{n+1/2,*}$. The second asterisk
 379 indicates that the obtained value of the momentum is due to receive a second correction as
 380 described below.

381 Note that (26) turns into a standard Poisson pressure projection equation for the pseudo-
382 incompressible cases when $\alpha = 0$. In these cases, the correction of P in (29) automatically
383 yields $P^{n+1} \equiv P_0$ up to the tolerance in the divergence term with which the Poisson equation
384 was solved. Thus, in the pseudo-incompressible cases, the pressure variable P is restored to
385 its background value as a result of the first correction as it should be.

386 Thus far we have stabilized the advecting fluxes by incorporating an implicit pressure
387 gradient contribution. We have not yet corrected the first-order error committed in the
388 predictor step for the momentum equation by using the old time level pressure. This task is
389 left to the second correction.

390 *Step 3: Second Correction*

391 The use of the old time level pressure in the momentum equation (21b) makes the predic-
392 tor step first order accurate w.r.t. momentum. In a second correction step, the pressure and
393 the momentum flux are corrected to achieve second-order accuracy and stability. Suppose we
394 have already calculated an appropriate pressure update $\delta p = p^{n+1} - p^n$, then the correction
395 of momentum reads

$$(\rho \mathbf{v})_C^{n+1} = (\rho \mathbf{v})_C^{n+1,**} - \frac{\Delta t}{2} \left(\tilde{\nabla} \cdot (\delta p \mathbf{I})_C + \mathbf{k} \sigma \delta p \right), \quad (30)$$

396 where

$$\sigma = (1 - \alpha) \beta \frac{g \rho_0}{\gamma p_0}. \quad (31)$$

397 Interpolating δp as computed in the first correction from the cell centers to the cell interfaces
398 and using these data to evaluate (30) turns out to generate an unstable update. We avoid
399 this by solving a second elliptic problem for a node-centered pressure variable (see similar
400 procedures in Almgren et al. (1998); Schneider et al. (1999); Klein (2009); Vater and Klein
401 (2009)). To derive the second elliptic equation, we multiply (30) by θ^{n+1} taking into account
402 that the scalars ρ, P, θ have already attained their final values after the first correction and

403 are unchanged in the second one. This yields

$$(P\mathbf{v})_C^{n+1} = (P\mathbf{v})_C^{n+1,**} - \frac{\Delta t}{2} \theta_C^{n+1} \left(\tilde{\nabla} \cdot (\delta p \mathbf{l})_C + \mathbf{k} \sigma \delta p \right). \quad (32)$$

404 As in the first correction we insert (32) into

$$\alpha \left(\frac{\partial P}{\partial t} \right)^{n+1/2} + \nabla \cdot \left(\frac{2-\alpha}{2} (P\mathbf{v})^{n+1} + \frac{\alpha}{2} (P\mathbf{v})^n \right) = 0, \quad (33)$$

405 where, for $\alpha = 1$, a second-order accurate midpoint discretization with no off-centering is
 406 considered. After node-centered space discretization of the divergence, we obtain the elliptic
 407 problem:

$$-\alpha \left(\frac{\mathcal{C}_H^{n+1}}{\Delta t} \delta p \right)_{\bar{C}} + \tilde{\nabla} \cdot \left(\frac{(2-\alpha)\Delta t}{4} \theta^{n+1} (\nabla \delta p + \mathbf{k} \sigma \delta p) \right)_{\bar{C}} = \tilde{\nabla} \cdot \left(\frac{2-\alpha}{2} (P\mathbf{v})^{n+1,**} + \frac{\alpha}{2} (P\mathbf{v})^n \right)_{\bar{C}}, \quad (34)$$

408 where \mathcal{C}_H^{n+1} is defined by (27) using the corrected value of P .

409 As in the first correction, we obtain a Helmholtz equation for $\alpha = 1$ where the zero-order
 410 term accounts for compressibility. The difference between FC ($\alpha = 1$) and $\text{PI}_{\rho,p}^{\text{tc}}$ ($\alpha = 0$) is
 411 a modified structure of the system matrix.

412 We note that in the fully-compressible case a backward difference (BDF2) discretization
 413 can be used, as done in Vater (2013). In that case, and for $\alpha = 1$, (34) is replaced with

$$-\left(\frac{3\mathcal{C}_H^{n+1}}{2\Delta t} \delta p \right)_{\bar{C}} + \frac{2}{3} \Delta t \tilde{\nabla} \cdot \left(\theta^{n+1} \tilde{\nabla} \delta p \right)_{\bar{C}} = \tilde{\nabla} \cdot (P\mathbf{v})_{\bar{C}}^{n+1} - \left(\frac{\mathcal{C}_H^{n+1}}{2\Delta t} \delta p^{\text{old}} \right)_{\bar{C}}, \quad (35)$$

414 where $\delta p^{\text{old}} = p^n - p^{n-1}$ denotes the old time level pressure increment.

415 A nine-point stencil is used for the discretization of the laplacian (34) or (35), which
 416 is obtained as follows: the nodal values define continuous piecewise bilinear pressure dis-
 417 tributions on the primary control volumes. We integrate their gradients analytically over
 418 the boundaries of the dual cells that are centered on the grid nodes. The solution δp is ac-
 419 cordingly defined in the centers of the dual cells, \bar{C} . Straightforward numerical integration
 420 of pressures over the primary cell interfaces can thus be employed in evaluating the second

421 momentum correction in (30). After the nodal pressures have been updated to the new time
422 level as well, all variables are now second-order accurate and ready for the next time step.
423 See details of the discretization in the Appendix.

424 4. Numerical Results

425 In this section, we present the results of the simulations performed with our semi-implicit
426 method. The aim is to show that the model numerics produces results in agreement with its
427 theoretical properties in different configurations. First, a convergence study in the FC config-
428 uration is presented. Then, results with fully-compressible (FC) and pseudo-incompressible
429 ($\text{PI}_{\rho,p}$) models are compared on simulations of thermal perturbations. The impact of the
430 thermodynamic consistency ($\text{PI}_{\rho,p}^{\text{tc}}$) term is also evaluated.

431 The numerical model is implemented in an object oriented C++ environment based on
432 the SAMRAI framework for mesh refinement (Hornung et al. 2006). Krylov-type methods
433 with algebraic multi-grid preconditioners as included in the Hypre library (Falgout et al.
434 2006) are used to solve the linear systems in the correction step. Our coding framework is
435 fully parallelized and 3d-ready. However, an extensive analysis of its parallel efficiency lies
436 outside the scope of the present work.

437 *Convergence study*

438 First, we assess the accuracy properties of the FC model on a case of pure transport
439 in a highly idealized setting with $g = 0$. The case (Kadioglu et al. 2008) consists of a
440 travelling rotating vortex in the doubly periodic unit-square-shaped domain $\Omega = [0, 1]^2 \text{ m}^2$.
441 The vortex is axisymmetric and rotates counterclockwise with unitary velocity. Density
442 is modelled by a smooth, non-constant function and a constant and a unitary transport
443 velocity $\mathbf{v} = (1, 1)^T \text{ m s}^{-1}$ is superimposed. The vortex is an exact solution for the zero
444 Mach number incompressible equations, to which $\text{PI}_{\rho,p}^{\text{tc}}$ and $\text{PI}_{\rho,p}$ reduce in the absence of

445 gravity (Klein 2009). With the pressure field correctly initialized, it is an exact solution for
 446 the fully-compressible equations as well. We refer to Kadioglu et al. (2008) for the initial
 447 data not reported here for brevity. Note that some of the coefficient in the expression for
 448 initial pressure were incorrectly reported in Kadioglu et al. (2008), the correct expression is
 449 available upon request.

450 In the compressible case, the initial distribution for P is derived via the equation of state
 451 (3). Reference physical quantities are set as follows:

$$\rho_{\text{ref}} = 0.5 \text{ kg m}^{-3}, p_{\text{ref}} = 101625 \text{ Pa}, T_{\text{ref}} = 706.098 \text{ K}, \quad (36)$$

452 corresponding to a maximum Mach number $M_{\text{max}} = \max(\|\mathbf{v}\|_{\text{RMS}}/\sqrt{\gamma p/\rho}) = 4.96\text{E-}03$. The
 453 high value of T_{ref} is computed from p_{ref} and ρ_{ref} considered in Kadioglu et al. (2008) and
 454 enables an easier comparison with their results for the density.

455 The flow is simulated by running the FC semi-implicit model ($\alpha \equiv 1$) on a grid with 192
 456 cells in both directions at CFL = 0.45, that is, constant $\Delta t = \Delta t_A = 9.7\text{E-}04$ s and $\Delta x =$
 457 $5.21\text{E-}03$ m. These data correspond to a sound-speed based $\text{CFL}_S = \text{CFL}/M_{\text{max}} \approx 90.72$.

458 The vortex is transported by the background unitary velocity. Due to the doubly periodic
 459 boundary, the initial configuration is reproduced unchanged at time $T = 1$ s (figure 2).
 460 Similar results (not shown) are obtained for momentum and P in FC runs and for all variables
 461 except for P (which is constant) in $\text{PI}_{\rho,p}^{\text{tc}}$ runs.

462 Furthermore, the numerical solution converges quadratically in the maximum norm (Fig-
 463 ure 3). The experimental order of accuracy is in agreement with the theoretical accuracy of
 464 the scheme presented in Section 3. Similar results are obtained with $\text{PI}_{\rho,p}^{\text{tc}}$ runs (not shown).

465 The FC results shown above validate the use of the fully-compressible flow solver that
 466 extends the pseudo-incompressible framework of Klein (2009).

468 Next, we consider a warm air bubble test case in the domain $\Omega = (x, z) \in [-10, 10] \times$
 469 $[0, 10]$ km². We set the following initial data for a homentropic atmosphere (Botta et al.
 470 2004):

$$p(z) = p_{\text{ref}} \left(1 - \Gamma \frac{g \rho_{\text{ref}}}{p_{\text{ref}}} z \right)^{\frac{1}{\Gamma}}, \quad \rho(z) = \rho_{\text{ref}} \left(\frac{p(z)}{p_{\text{ref}}} \right)^{\frac{1}{\gamma}}, \quad \rho_{\text{ref}} = \frac{p_{\text{ref}}}{RT_{\text{ref}}}, \quad (37)$$

471 where, in agreement with Klein (2009), ρ_{ref} , p_{ref} , g , and T_{ref} have the values 1 kg m^{-3} ,
 472 $8.61\text{E}04 \text{ N m}^{-2}$, 10 m s^{-2} , and 300 K , respectively, and $\Gamma = (\gamma - 1)/\gamma$. The background
 473 potential temperature θ is constant. The homentropic setting (37) is perturbed with a
 474 smoothed cone-shaped thermal perturbation θ' , given by (Klein 2009):

$$\theta'(x, z) = \begin{cases} \delta\theta \cos^2(\frac{\pi}{2}r) & (r \leq 1) \\ 0 & \text{otherwise} \end{cases}, \quad \begin{cases} \delta\theta = 2 \text{ K} \\ r = 5\sqrt{(\frac{x}{L})^2 + (\frac{z}{L} - \frac{1}{5})^2} \\ L = 10 \text{ km} \end{cases}. \quad (38)$$

475 The initial velocity is zero. Lateral boundary conditions are periodic, with solid walls on top
 476 and bottom boundaries.

477 We run our semi-implicit trapezoidal scheme on a grid with $\Delta x = \Delta z = 125 \text{ m}$, i.e.
 478 160×80 cells, and $\text{CFL} = 0.5$. In the first five steps a buoyancy-driven time step ($\Delta t =$
 479 $\Delta t_{\text{B}} \approx 21.69 \text{ s}$) is used. Due to growing velocities, the advection-driven time step is used for
 480 the remainder of the simulation. Towards the end of the simulation, values of $\Delta t \approx 4.6 \text{ s}$ are
 481 attained.

482 Driven by buoyancy, the warm bubble rises and rolls up on the sides (figure 4). The
 483 amplitude of the thermal perturbation at final time $T = 1000 \text{ s}$ is in agreement with the
 484 results in Klein (2009), as shown in table 2. However, the $\text{PI}_{\rho,p}$ bubble rises faster, is not as
 485 wide and exhibits a phase shift with respect to both the $\text{PI}_{\rho,p}^{\text{tc}}$ and the FC models (figure 5).

486 The discrepancies in the $\text{PI}_{\rho,p}$ model come from neglecting the effect of pressure per-
 487 turbations on the buoyancy. The extra buoyancy term present in the $\text{PI}_{\rho,p}^{\text{tc}}$ model reduces
 488 buoyancy near the top of the bubble due to an increase in pressure near the bubble top and

489 increases buoyancy at the two tails due to a pressure decrease near the tails. Furthermore,
 490 the overall buoyancy of the bubble decreases causing a decrease in the phase speed. There-
 491 fore the $\text{PI}_{\rho,p}^{\text{tc}}$ bubble is both lower and wider than the $\text{PI}_{\rho,p}$ model and, as a result, resembles
 492 the FC model more closely.

493 Results with $\text{PI}_{\rho,p}^{\text{tc}}$ as measured in a one-dimensional cut of θ' at height $z = 7500$ m match
 494 the FC results within a 2 per cent error (table 3).

495 Results with the $\text{PI}_{\rho,p}^{\text{tc}}$ model do not differ substantially from FC results at the end of
 496 the simulation at $T = 1000$ s. The different dynamics of the FC case can be detected in the
 497 onset of sound waves in the initial stages of the simulation. With the FC model ($\alpha = 1$) the
 498 initial potential temperature perturbation triggers acoustic waves. These are visible in the
 499 upper left panel of Figure 6, which displays pressure increments at time $t = 26.6$ s in a run
 500 of the FC model with $\Delta t = \Delta t_{\text{I}} = 1.9$ s. The oscillations are due to the initial hydrostatic
 501 pressure distribution from (37) not being acoustically balanced.

502 The presence of associated pressure oscillations is confirmed by a time series over the
 503 first 350 s of the pressure time increment values recorded at the point $(x, z) = (-7.5, 5)$ km
 504 marked with a cross in the upper left panel of Figure 6. The time series are shown in the
 505 upper right, lower left and lower right panels of Figure 6. The upper right and lower left
 506 plots are relative to simulations at constant $\Delta t = \Delta t_{\text{I}} = 1.9$ s. The simulation relative to
 507 the lower right panel is at $\text{CFL} \approx 0.5$ as in Figure 4.

508 FC model results (solid lines in all plots) display oscillations triggered by the initial
 509 pressure imbalance. The amplitude of the acoustic oscillations in the small time step case
 510 (upper right panel) is ninefold the amplitude of the large time step runs (lower right panel).
 511 The effect is suppressed in the $\text{PI}_{\rho,p}$ runs (dashed lines) except for an initial transient. Note
 512 that in the large-time step run the initial transient masks the amplitude of the acoustics.
 513 Therefore, the data of the first time step was removed in the lower right panel of Figure 6.

514 In the case of the $\text{PI}_{\rho,p}$ model, pressure is determined by the solution of a time-independent
 515 Poisson problem, which describes the pressure field in the absence of sound waves. $\text{PI}_{\rho,p}$ is

516 considered here because the extra $\text{PI}_{\rho,p}^{\text{tc}}$ term does not modify the results as far as acoustics
 517 are concerned. On the one hand, the reduction in the amplitude of the large time step acous-
 518 tic oscillations shows that the semi-implicit method is able to handle acoustic oscillations at
 519 CFL numbers independent of the sound speed. On the other hand, the effect of acoustics is
 520 not completely suppressed in the large-time step, either.

521 However, thanks to the blending feature, the code is able to continuously transition from
 522 the $\text{PI}_{\rho,p}$ configuration to the FC configuration. The lower left panel of Figure 6 shows the
 523 time series of pressure increments for blended runs. We set the transition parameter α from
 524 section 2 to zero for S_1 time steps. Then, α increases linearly to $\alpha = 1$ over S_2 time steps.
 525 Starting at the time step number $S_1 + S_2$, the code runs compressibly with $\alpha = 1$.

526 In the lower left panel of Figure 6, the thin solid line in the background denotes the
 527 fully-compressible run. The dashed-dotted curve and thick solid curves were obtained with
 528 $S_2 = 20$ and $S_2 = 40$, respectively. There are no disturbances for the first $S_1 = 10$ pseudo-
 529 incompressible steps in these two pressure graphs, and the results coincide with those from
 530 the run of the $\text{PI}_{\rho,p}$ model (dashed line in the right panels). Perturbations arise in the
 531 transitional period and fully develop after $S_1 + S_2$ time steps. The oscillations' amplitudes
 532 in the blended runs are considerably lower than those of the FC run and they are lower for
 533 the larger S_2 value, i.e. the longer transitional period.

534 Results in the lower left panel of figure 6 demonstrate the capabilities of the blended
 535 model. Acoustic perturbations are absent when the model runs in pseudo-incompressible
 536 mode with $\alpha = 0$ and they emerge significantly damped after the transition to $\alpha = 1$
 537 in fully-compressible mode. Therefore, when blended continuously with the compressible
 538 discretization, the soundproof limit discretization can be used to actively control imbalances
 539 in the initial data. The oscillation amplitudes are substantially reduced also when larger
 540 time steps are employed as seen in the lower right panel of figure 6.

541 Finally, as in Almgren et al. (2006a), which presents a pseudo-incompressible code for
 542 stellar hydrodynamics, we compare plots of the Mach number in the initial stages of FC,

543 $PI_{\rho,p}$ and blended runs. Results at time $t = 21.66$ s, that is, time step number 57 at
544 $\Delta t = \Delta t_I = 0.38$ s, are displayed in Figure 7. The mushroom-shaped FC result (left panel)
545 reveals the initial onset of sound waves due to pressure imbalances already inspected in Figure
546 6, while the $PI_{\rho,p}$ plot (middle panel) and blended plot (right panel) show no perturbation
547 away from the bubble. A very small time step was considered in this case following Almgren
548 et al. (2006a) in order to track more closely the dynamics in the initial stages.

549 *Density current*

550 This test (Straka et al. 1993) consists of a negative potential temperature perturbation
551 in a $[-25.6, 25.6] \times [0, 6.4]$ km² homentropic atmosphere (37),

$$T' = \begin{cases} 0 \text{ K} & \text{if } r > 1 \\ -15 [1 + \cos(\pi r)] / 2 \text{ K} & \text{if } r < 1 \end{cases}, \quad (39)$$

552 where $r = \{[(x - x_c)/x_r]^2 + [(z - z_c)/z_r]^2\}^{0.5}$, $x_c = 0$ km, $x_r = 4$ km, $z_c = 3$ km and
553 $z_r = 2$ km. From $\theta = T(p/p_{\text{ref}})^{-\Gamma}$ we derive the potential temperature perturbation and
554 density distribution,

$$\theta'(x, z) = \frac{T'}{1 - \Gamma \frac{g p_{\text{ref}}}{p_{\text{ref}}} z}, \quad \rho(z) = \rho_{\text{ref}} \left(\frac{p(z)}{p_{\text{ref}}} \right)^{\frac{1}{\gamma}} \frac{\theta_{\text{ref}}}{\theta_{\text{ref}} + \theta'}, \quad (40)$$

555 where $\theta_{\text{ref}} = T_{\text{ref}}$. The boundary conditions are periodic on the left and right boundary, solid
556 walls on the top and bottom boundary. Furthermore, we add an artificial diffusion term
557 $\rho\mu\nabla^2\mathbf{v}$ to the right hand side of the momentum equation ($\rho\mu\nabla^2\theta$ in the P equation), with
558 $\mu = 75$ m² s⁻¹ as in Straka et al. (1993). The initial velocity is set to zero, and the reference
559 quantities are $T_{\text{ref}} = 300$ K, $p_{\text{ref}} = 10^5$ Pa, $\rho_{\text{ref}} = p_{\text{ref}}/(RT_{\text{ref}})$.

560 The models are run with $\Delta x = 50$ m and CFL = 0.5. Thus, the time step is $\Delta t = \Delta t_B \approx$
561 4.65 s for the first three steps and then the advective time step is used. For the FC model, a
562 backward difference approach in the second projection is used, see equation (35). Due to the
563 symmetrical nature of the test case, only the plots for the subdomain $[0, 19.2] \times [0, 4.8]$ km²
564 are shown.

565 Obtained values of the final thermal perturbation and the front positions as calculated
566 by the FC and $\text{PI}_{\rho,p}^{\text{tc}}$ models (Figure 8 and table 4) are in line with results in the literature
567 (Straka et al. 1993; Restelli and Giraldo 2009). In contrast to the rising bubble case, the
568 extra buoyancy term in the $\text{PI}_{\rho,p}^{\text{tc}}$ model results in an overall increase in the buoyancy of the
569 bubble. This increase in buoyancy causes the bubble to fall slower and reduces the phase
570 speed when compared with the $\text{PI}_{\rho,p}$ model. This can be seen in the farther front position and
571 in the horizontal cut at height $z = 1200$ m (Figure 9) of the $\text{PI}_{\rho,p}$ model when compared to
572 both the FC and $\text{PI}_{\rho,p}^{\text{tc}}$ models. As a result, the $\text{PI}_{\rho,p}$ model displays considerable deviations
573 (higher than 40 per cent) relative to FC runs (Table 5). For the $\text{PI}_{\rho,p}^{\text{tc}}$ model, the deviation
574 from FC is lower than 5 per cent.

575 *Inertia-gravity waves*

576 Next, we consider a thermally stratified atmosphere with stable stratification of potential
577 temperature $\partial\theta/\partial z > 0$. In particular, as in Restelli and Giraldo (2009); Skamarock and
578 Klemp (1994), we take:

$$\theta(z) = T_{\text{ref}} \exp\left(\frac{N^2}{g} z\right), \quad (41)$$

579 where N denotes the buoyancy frequency. With $N = 0.01 \text{ s}^{-1}$, $g = 9.81 \text{ m s}^{-2}$, and $T_{\text{ref}} =$
580 300 K , we have $\theta \in [300, 332.19] \text{ K}$ for $z \in [0, 10] \text{ km}$. The other variables are defined as:

$$p(z) = p_{\text{ref}} \left\{ 1 - \frac{g}{N^2} \Gamma \frac{g \rho_{\text{ref}}}{p_{\text{ref}}} \left[1 - \exp\left(-\frac{N^2 z}{g}\right) \right] \right\}^{\frac{1}{\Gamma}}, \quad (42)$$

$$\rho(z) = \rho_{\text{ref}} \left(\frac{p(z)}{p_{\text{ref}}} \right)^{\frac{1}{\gamma}} \exp\left(-\frac{N^2 z}{g}\right), \quad \rho_{\text{ref}} = \frac{p_{\text{ref}}}{RT_{\text{ref}}}, \quad (43)$$

581 with $p_{\text{ref}} = 10^5 \text{ Pa}$. On top of the background stratification (41)–(42), in a $[0, 300] \times [0, 10] \text{ km}^2$
582 domain we consider the perturbation (Skamarock and Klemp (1994) and Figure 10 left
583 panel):

$$\theta'(x, z, 0) = 0.01 \text{ K} * \frac{\sin(\pi z/H)}{1 + [(x - x_c)/a]^2} \quad (44)$$

584 with $H = 10$ km, $x_c = 100$ km, $a = 5$ km. In addition, there is a background horizontal
 585 flow $u = 20$ m s⁻¹. The simulations are performed with at advective CFL = 0.3, that is
 586 $\Delta t = \Delta t_A \approx 3.75$ s. The grid spacing is $\Delta x = \Delta z = 250$ m and the trapezoidal time
 587 integrator is employed for the FC model. In agreement with published work (Restelli and
 588 Giraldo 2009), the Coriolis term is neglected here because of the small length of the channel.

589 Unlike the previous test cases, here the dynamics is chiefly wavelike rather than vertically
 590 buoyancy-driven. Inertia-gravity waves develop in the horizontal direction (Figure 10). As
 591 in the previous test case, only the FC contour plots are presented in Figure 10 as the $\text{PI}_{\rho,p}^{\text{tc}}$
 592 and $\text{PI}_{\rho,p}$ plots are visually indistinguishable.

593 A quantitative comparison between the FC, $\text{PI}_{\rho,p}^{\text{tc}}$ and $\text{PI}_{\rho,p}$ results and the results of
 594 Restelli and Giraldo (2009) is reported in table 6. Maxima and minima of perturbations of
 595 velocity components, potential temperature and Exner pressure at final time $T = 3000$ s are
 596 in line with published work.

597 The left panel of Figure 11 shows a one-dimensional cut of the potential temperature
 598 perturbation at $z = 5000$ m. As in the previous cases, the $\text{PI}_{\rho,p}$ model displays a higher
 599 phase speed than the $\text{PI}_{\rho,p}^{\text{tc}}$ and FC models due to the neglect of pressure perturbations in
 600 the buoyancy term. The region of the leftmost crest is magnified in Figure 11 to highlight
 601 the difference in the phase speed of the $\text{PI}_{\rho,p}$ model (dashed-dotted line) with respect to the
 602 $\text{PI}_{\rho,p}^{\text{tc}}$ model (starred markers) and the FC model (solid line).

603 The right panel of Figure 11 shows the differences between the FC cut and the $\text{PI}_{\rho,p}^{\text{tc}}$ cut
 604 (dashed line) and between the FC cut and the $\text{PI}_{\rho,p}$ cut (solid line). The amplitude of the
 605 difference is larger in the latter case due to the phase shift highlighted on the left panel. The
 606 result is quantified in Table 7 which shows relative RMS and max errors of the FC cut with
 607 respect to the $\text{PI}_{\rho,p}^{\text{tc}}$ and $\text{PI}_{\rho,p}$ cuts. Relative $\text{PI}_{\rho,p}$ -FC errors are threefold the $\text{PI}_{\rho,p}^{\text{tc}}$ -FC ones

608 Finally, as in Restelli and Giraldo (2009) we define conservation errors as:

$$C_\phi = \frac{|(\phi_{\text{tot}})_T - (\phi_{\text{tot}})_0|}{(\phi_{\text{tot}})_0}, \quad (45)$$

609 where $\phi_{\text{tot}} = \int_\Omega \phi d\mathbf{x}$ denotes the volumetric integral of ϕ in the domain Ω . Subscripts 0

610 and T denote initial and final time, respectively. We expect our scheme to conserve density
 611 ρ and horizontal momentum density ρu . Though our model does not conserve total energy
 612 ρE , we report conservation scores for that variable, too. For the FC model, results for P are
 613 also reported. Values of the conservation error for ρ , ρu , P , and ρE are fairly low for the
 614 three model configurations (table 8). Note, in table 8 we define the total energy variable as

$$E = \frac{1}{\rho} \frac{p}{\gamma - 1} + \frac{\mathbf{v}^2}{2} + gz. \quad (46)$$

615 where $p = p_0$ in (46) for the $\text{PI}_{\rho,p}^{\text{tc}}$ and $\text{PI}_{\rho,p}$ cases as shown in Klein and Pauluis (2011).
 616 Numerical analysis of the P -conservation is only meaningful for the FC model, since in the
 617 incompressible cases $P = P_0(z)$ holds.

618 5. Discussion and conclusions

619 We have presented a blended weakly compressible computational model with seamless
 620 access to thermodynamically consistent pseudo-incompressible dynamics, these two repre-
 621 senting the limiting cases of a family of models depending on one parameter. For each
 622 member of the model family, the numerical discretization is the same up to certain weights
 623 in the stencil of the implicit corrector invoked to enable advection-based time steps in sim-
 624 ulations of small to mesoscale systems.

625 This seamless and straightforward compressible-to-soundproof model transition can be
 626 realized in any flow solver that features the density and the mass-weighted potential temper-
 627 ature as prognostic variables for the thermodynamics, together with flux-based formulations
 628 of their determining equations. Weak checkerboard modes were observed in the runs of
 629 gravity-driven flows for very small time steps. We attribute them to the fact that the diver-
 630 gence of the cell-centered velocity is controlled in the second correction through a discrete
 631 elliptic problem derived from the linearized acoustic equations on the Arakawa B-Grid with
 632 a standard stencil. This grid arrangement allows for oscillatory modes with phase vectors
 633 pointing roughly along the grid diagonals (see Figure 8 of Arakawa and Lamb (1977)). These

634 modes might be controllable by adopting a staggered grid arrangement (Arakawa C-grid)
635 or by adopting an inf-sup stable discretization of the elliptic operator on the B-Grid as in
636 Vater and Klein (2009).

637 The key observation enabling the blending is that, at least for an ideal gas with constant
638 specific heat capacities, $\rho\theta$ is a function of pressure alone. Thus the transport equation for
639 $\rho\theta$ is equivalent to the pressure evolution equation and lends itself naturally for implicit
640 pressure formulations. Once available, such a seamless framework can be used, e.g., for a
641 clean comparison of compressible and soundproof models that is not affected by sizeable
642 differences between the respective model discretizations (see Smolarkiewicz and Dörnbrack
643 (2008); Smolarkiewicz et al. (2014) for comparable arguments).

644 As a further potentially attractive application of such a modeling tool we suggest the
645 filtering of unbalanced initial data. For given initial data, a matching pressure field and a
646 related divergence correction that would guarantee a nearly sound-free subsequent evolution
647 are generally not available. With a blended soundproof-compressible framework, one can
648 generate accurate balanced pressure and velocity fields by running the model in soundproof
649 mode for a few time steps and then making the transition to fully-compressible over another
650 few steps. This idea may also be transferred to other nearly balanced situations, such as
651 hydrostatic and geostrophic, but exploring this is left for future work. In the framework
652 of techniques for atmospheric data assimilation (Rabier 2005), the resulting ability of a
653 computational model to manage and regularly embed new, unbalanced input in a balanced
654 fashion and without invoking additional filtering procedures appears quite attractive. This
655 capability can also be more generally useful when one has to map externally obtained data
656 into a multi-dimensional finite volume scheme as analyzed in Zingale et al. (2002).

657 Besides the aforementioned blending features, there are other noteworthy aspects of the
658 scheme. First, we discretize the equations in full form without subtraction of a background
659 state, maintaining accuracy by adopting a well-balanced discretization of the pressure gradi-
660 ent and gravity terms as discussed in Botta et al. (2004); Klein (2009). Second, we cast the

661 momentum equation in terms of pressure and density instead of the more common Exner
662 pressure and potential temperature. The former choice guarantees conservation of momen-
663 tum in the absence of external forces and increases flexibility with a view to implementing
664 more general equations of state (Klein and Pauluis 2011).

665 Code performance was assessed in a number of configurations. The second-order accuracy
666 of the scheme was verified on a smooth benchmark. Then, standard test cases consisting
667 of buoyant thermal perturbations were considered, where our data confirmed no substan-
668 tial difference between the compressible and pseudo-incompressible results. For the latter,
669 including the linearized effect of pressure on density in the gravity term results not only in
670 thermodynamic consistency (Klein and Pauluis 2011) but also in improved accuracy. Our
671 findings are consistent with Davies et al. (2003); Klein et al. (2010), thus confirming the
672 validity of the pseudo-incompressible model at small to mesoscales and for realistic stratifi-
673 cations.

674 As mentioned, we are planning to extend the present general strategy to include addi-
675 tional dominant balances relevant for larger scale flows, specifically to the hydrostatic and
676 geostrophic limits. This goal appears feasible in view of recent related work. For example,
677 successful results have been achieved by EULAG model users (Prusa and Gutowski 2011;
678 Szmelter and Smolarkiewicz 2011; Smolarkiewicz et al. 2014) with compressible, anelastic,
679 and pseudo-incompressible models on the synoptic and planetary scales. Furthermore, al-
680 ternatives have been explored to merge hydrostatic models with fully-compressible (Janjic
681 et al. 2001) or soundproof ones. Careful consideration will be needed to identify the correct
682 large-scale limiting model in the light of recent suggestions of unified multiscale reduced
683 models by Durran (2008) and Arakawa and Konor (2009); Konor (2014).

684 *Acknowledgments.*

685 The authors thank Matthias Waidmann, Stephan Gerber, and Michael Oevermann for the
686 fluid solver software this work is based upon. We thank the SAMRAI developers at Lawrence

687 Livermore National Laboratory for their ingenious adaptive mesh refinement framework.
688 Hilary Weller, Ronny Petrik, and another anonymous referee have helped us improving our
689 work and presentation through numerous constructive comments. The same holds for Piotr
690 Smolarkiewicz and Luca Bonaventura with whom we have also shared ideas along the way.
691 We thank Deutsche Forschungsgemeinschaft for support through the Berlin Mathematical
692 School, and grants KL 611/23-1,2 (“MetStröm”). T. Benacchio and R. Klein greatly appreci-
693 ated the opportunity to work for several weeks in the stimulating environment of the Newton
694 Institute, Cambridge, UK, during the fall of 2012, and R. Klein acknowledges the support
695 of the National Center for Atmospheric Research, Boulder, Co., for financially supporting
696 several research visits.

Details of the numerical scheme

700 Here we elaborate on the aspects of the numerical scheme omitted in the main text.

701 *Predictor*

702 We use a second-order accurate, explicit two-stage strong stability-preserving Runge-Kutta
703 method for time integration (Gottlieb et al. 2001). For the Ordinary Differential Equation:

$$\frac{du}{dt} = L(u), \quad (\text{A1})$$

704 where L denotes a differential operator, the method reads:

$$u^{(1)} = u^n + \Delta t L(u^n), \quad (\text{A2})$$

$$u^{n+1} = \frac{1}{2}u^n + \frac{1}{2}u^{(1)} + \frac{1}{2}\Delta t L(u^{(1)}), \quad (\text{A3})$$

705 where $u^{(1)}$ denotes the first stage solution.

706 The spatial discretization is performed with a finite volume approach, see, e.g., LeVeque
707 (2002). Discrete variables are defined as approximations of cell averages set at cell centers,
708 with the exception of dynamic pressure, set at cell nodes. The new cell-centered values are
709 obtained from the old ones subtracting the net outflow flux at the boundaries and adding
710 the contribution from the source term, expressions (21a)–(21b)–(21c) in the main text.

711 The discretization of the fluxes is performed according to the following steps:

- 712 i. The velocity at the interfaces is determined by averaging the neighbouring leftmost
713 and rightmost cell-centered values \mathbf{v}_L and \mathbf{v}_R :

$$\mathbf{v} = \frac{1}{2}(\mathbf{v}_L + \mathbf{v}_R), \quad (\text{A4})$$

714 where, for a second-order method, \mathbf{v}_L and \mathbf{v}_R have to be linearly reconstructed/limited.
 715 Considering the interface $(x_{i+1/2}, y_j)$, and omitting the subscript j for simplicity, the
 716 reconstructed values of the horizontal velocity u are:

$$u_L = u_i + \frac{1}{2}\psi(u_i - u_{i-1}, u_{i+1} - u_i), \quad (\text{A5})$$

$$u_R = u_{i+1} - \frac{1}{2}\psi(u_{i+1} - u_i, u_{i+2} - u_{i+1}), \quad (\text{A6})$$

717 where:

$$\psi(a, b) = \frac{a + b}{2} \quad (\text{A7})$$

718 for centered slopes. Our implementation features also an option for slope limiters, for
 719 which ψ would have a different functional form. Upwind fluxes F_P for the P variable
 720 are computed by means of the obtained velocity:

$$F_P = F_P^+ + F_P^-, \quad (\text{A8})$$

721 where:

$$F_P^+ = P_L \max(\mathbf{v}, 0), \quad F_P^- = P_R \min(\mathbf{v}, 0), \quad (\text{A9})$$

722 and the subscripts L and R denote cell-centered leftmost and rightmost values of the
 723 variable.

724 ii. Fluxes for the remaining quantities are referred to the carrier flux $P\mathbf{v}$ and derived
 725 using (A9) as

$$F_\phi = F_P^+ \phi_L + F_P^- \phi_R \quad (\text{A10})$$

726 where $\phi \in \{1/\theta, \mathbf{v}/\theta\}$. The contribution from the pressure term is incorporated in the
 727 momentum flux adding the pressure value at the center of the cell interface, obtained
 728 via average of the adjacent nodal values.

729 *Pressure update*

730 The nodal pressure update at the end of the time step proceeds as follows:

731 i. An auxiliary cell-centered pressure p_c is computed from P using the inverse of the
 732 equation of state (2). The result is then interpolated to the nodes:

$$p_c^{n+1} = \left(\frac{P^{n+1,**}}{\rho_{ref} T_{ref}} \right)^\gamma p_{ref} - p_{ref}, \quad p_c^{n+1} \longrightarrow p_{\text{EOS}}^{n+1}. \quad (\text{A11})$$

733 ii. The obtained value is weighted with the old time level pressure update with the solution
 734 of (34) or (35), δp :

$$p^{n+1} = \alpha p_{\text{EOS}}^{n+1} + (1 - \alpha) (p^n + \delta p). \quad (\text{A12})$$

735 When the model runs in pseudo-incompressible mode with $\alpha = 0$, the node-centered pressure
 736 increment δp is summed to the old time level value. In compressible mode, with $\alpha = 1$, the
 737 new nodal pressure is locked to P imposing the equation of state at a discrete level.

738 Other solutions are possible and were tested. For example, as a pseudo-incompressible
 739 update, an interpolated value of the solution δp_c of the first correction equation (26) can be
 740 summed to the old time level pressure value. This was used in the thermal perturbations
 741 simulated with the fully-compressible model initially run in pseudo-incompressible mode.
 742 In that case the solution of the second Poisson problem only serves as a correction to the
 743 momentum flux, expression (30), not as an update for the nodal pressure value.

744 *Time step choice*

745 The explicit time integration method adopted in the predictor step must be consistent with
 746 the CFL stability condition for advection (Courant et al. 1928), and a similar constraint
 747 for internal wave dynamics since these processes are handled explicitly in our scheme. In
 748 particular, we dynamically compute the time step size at each time loop according to:

$$\Delta t = \min(\Delta t_I, \Delta t_A, \Delta t_B) \quad (\text{A13})$$

749 where Δt_I is an externally imposed value of the time step. Δt_A is the advective time step:

$$\Delta t_A = \frac{\text{CFL} \Delta x}{\max_{\Omega} (\|\mathbf{v}\|_2)}, \quad (\text{A14})$$

750 where $\text{CFL} \leq 1$ and $\|\cdot\|_2$ is the discrete L^2 norm. Δt_B is a buoyancy-dependent time step:

$$\Delta t_B = \text{CFL} \sqrt{\frac{\Delta x \min_{\Omega} \theta}{g \max_{\Omega} \Delta \theta}}, \quad (\text{A15})$$

751 where $\max_{\Omega} \Delta \theta = \max_{\Omega} \theta - \min_{\Omega} \theta$ is the maximum potential temperature perturbation.

752 Dynamically adaptive time stepping is standard on computational fluid dynamics and for

753 two time level schemes it's implementation is quite straightforward (LeVeque 2002).

754 *Well-balanced treatment of vertical pressure gradient and gravity term*

755 In the envisaged atmospheric applications, flow patterns arise as perturbations around a

756 hydrostatically balanced state, where the vertical pressure gradient offsets the gravitational

757 force

$$\frac{\partial p}{\partial z} = -\rho g. \quad (\text{A16})$$

758 Therefore, an essential characteristic of a numerical method in this context is the capabil-

759 ity of mimicking the hydrostatic balance at the discrete level. This means, for instance, that

760 the numerical discretization should introduce no perturbations on an initially motionless at-

761 mospheric setting. The feature is especially nontrivial for models as the ones presented here

762 whose analytical formulation relies on full variables, unlike other non-hydrostatic fully com-

763 pressible models (e.g., Skamarock and Klemp (2008); Restelli and Giraldo (2009)) wherein

764 the unknowns are themselves perturbations around a background hydrostatically balanced

765 reference state.

766 Here we adopt the approach of Botta et al. (2004), who describe the implementation of

767 a discrete Archimedes' principle, and in the following we present the parts of our implemen-

768 tation tuned to take into account the hydrostatic balance.

770 Since the problem is inherently one-dimensional, we focus on the vertical coordinate for
 771 the moment. First, let the initial data for pressure $p(z)$ and density $\rho(z)$ be given in the
 772 form of a homentropic or stably stratified atmosphere as in expressions (37) or (42) above.
 773 Next:

- 774 • $p(z)$ is initialized in cell centres z_j , $j = 1, \dots, \mathcal{N}_z$ and nodes $z_{j-1/2}$, $j = 1, \dots, \mathcal{N}_z + 1$
 775 according to its analytical expression (37) or (42);
- 776 • $\rho(z)$ is initialized at z_j using a discretized form of (A16), i.e.

$$\rho(z_j) = -\frac{1}{g\Delta z}[p(z_{j+1/2}) - p(z_{j-1/2})], \quad j = 1, \dots, \mathcal{N}_z. \quad (\text{A17})$$

777 where Δz is the vertical grid spacing.

778 *Predictor step*

779 The value of the pressure at the center of the cell face needed for the momentum flux
 780 computation in expression (19b) is computed as follows:

$$p(z_j) = \frac{1}{2} \{p(z_{j+1/2}) + p(z_{j-1/2}) - g [2f(z_j) - f(z_{j+1/2}) - f(z_{j-1/2})]\} \quad (\text{A18})$$

781 for $j = 1, \dots, \mathcal{N}_z$, where:

$$f(z) = \int_0^z \rho(z') dz' \quad (\text{A19})$$

782 and the square bracket in (A18) represents a hydrostatic modification of the simple average.

783 *Boundary conditions*

784 The so-called “solid wall” boundary conditions are adjusted to take into account hydro-
 785 static balance. As customary in finite differences and finite volume codes (LeVeque 2002),

786 we implement fully reflecting boundaries using “ghost cells”. The strategy involves attach-
 787 ing two dummy cells to the boundary in which the value of all the variables except for the
 788 normal velocity is mirrored from the two innermost cells, whereas the normal velocity value
 789 is taken with opposite sign.

790 We modify the process for the mirrored variables in that we retrieve in the ghost cells
 791 the hydrostatically-consistent values. For instance, for the pressure in the first lower ghost
 792 cell (cell 0) we have:

$$p_{z_0} = p(z_1) + g \int_{z_0}^{z_1} \rho(z) dz \quad (\text{A20})$$

793 and similar expressions hold for the upper values.

794 *Final locking of pressure and P variables*

795 The third modification involves the interpolation from nodes to cell centers or *vice versa*,
 796 which in the case without gravity is a standard linear interpolation. Here, a correction taking
 797 into account hydrostaticity is introduced. In particular, for the cell-to-node interpolation
 798 used in the pressure update (A11) after the second correction step:

- 799 • For the lower boundary nodes:

$$p(x_{i+1/2}, z_{1/2}) = 0.5(p_{NW} + p_{NE}), \quad \forall i = 1, \dots, \mathcal{N}_x \quad (\text{A21})$$

800 where p_{NW} and p_{NE} denote the pressure values obtained with analytical integration
 801 downwards from the hydrostatic pressure values in the adjacent upper left and upper
 802 right cell, respectively.

- 803 • For the upper boundary nodes:

$$p(x_{i+1/2}, z_{\mathcal{N}_z+1/2}) = 0.5(p_{SW} + p_{SE}), \quad \forall i = 1, \dots, \mathcal{N}_x \quad (\text{A22})$$

804 where p_{SW} and p_{SE} denote the pressure values obtained with analytical integration
 805 upwards from the hydrostatic pressure values in the adjacent lower left and lower right
 806 cell, respectively.

807

- For the internal nodes:

$$p(x_{i+1/2}, z_{j+1/2}) = 0.25(p_{SW} + p_{SE} + p_{NW} + p_{NE}), \quad \forall i = 1, \dots, \mathcal{N}_x, j = 1, \dots, \mathcal{N}_z - 1$$

(A23)

808

Finally, we remark that issues due to neglect of hydrostatic balance at the discrete level

809

manifest less in the incompressible than in the fully-compressible version of our method.

810

In the former, small spurious perturbations due to inexact balancing, for instance, at the

811

boundary are projected away in the correction step, while in the latter P and pressure are

812

locked through the equation of state, thus requiring a careful adjustment.

REFERENCES

- 815 Achatz, U., R. Klein, and F. Senf, 2010: Gravity Waves, Scale Asymptotics and the Pseudo-
816 Incompressible Equations. *J. Fluid Mech.*, **663**, 120–147.
- 817 Almgren, A. S., J. B. Bell, P. Colella, L. H. Howell, and M. L. Welcome, 1998: A conser-
818 vative adaptive projection method for the variable density incompressible Navier-Stokes
819 equations. *J. Comput. Phys.*, **142**, 1–46.
- 820 Almgren, A. S., J. B. Bell, C. A. Rendleman, and M. Zingale, 2006a: Low Mach number
821 modeling of type Ia supernovae. I. Hydrodynamics. *Astrophys. J.*, **637**, 922–936, doi:
822 10.1086/498426.
- 823 Almgren, A. S., J. B. Bell, C. A. Rendleman, and M. Zingale, 2006b: Low Mach number
824 modeling of type Ia supernovae. II. Energy evolution. *Astrophys. J.*, **649**, 927–938.
- 825 Arakawa, A. and C. S. Konor, 2009: Unification of the anelastic and quasi-hydrostatic
826 systems of equations. *Mon. Wea. Rev.*, **137**, 710–726.
- 827 Arakawa, A. and V. R. Lamb, 1977: Computational design of the basic dynamical processes
828 of the UCLA general circulation model. *Methods Comput. Phys.*, **17**, 173–265.
- 829 Bannon, P. R., 1996: On the anelastic approximation for a compressible atmosphere. *J.*
830 *Atmos. Sci.*, **53**, 3618–3628.
- 831 Bell, J., L. Howell, and P. Colella, 1991: An efficient second-order projection method for
832 viscous incompressible flow. *10th AIAA Computational Fluid Dynamics Conference, Hon-*
833 *olulu, June 24-27, 1991.*
- 834 Bijl, H. and P. Wesseling, 1998: A unified method for computing incompressible and com-
835 pressible flows in boundary-fitted coordinates. *J. Comput. Phys.*, **141**, 153–173.

836 Bonaventura, L., 2000: A semi-implicit semi-Lagrangian scheme using the height coordinate
837 for a nonhydrostatic and fully elastic model of atmospheric flows. *J. Comput. Phys.*, **158**,
838 186–213.

839 Botta, N., R. Klein, S. Langenberg, and S. Lützenkirchen, 2004: Well balanced finite volume
840 methods for nearly hydrostatic flows. *J. Comput. Phys.*, **196**, 539–565.

841 Brdar, S., M. Baldauf, A. Dedner, and R. Klöfkorn, 2013: Comparison of dynamical cores for
842 NWP models: comparison of COSMO and Dune. *Theor. Comp. Fluid Dyn.*, **27**, 453–472.

843 Casulli, V. and D. Greenspan, 1984: Pressure correction method for the numerical solution
844 of transient compressible fluid flows. *Int. J. Num. Meth. Fluids*, **4**, 1001–1012.

845 Courant, R., K. Friedrichs, and H. Lewy, 1928: Über die partiellen Differenzgleichungen
846 der mathematischen Physik. *Math. Ann.*, **100**, 32–74.

847 Cullen, M. J. P., 2007: Modelling atmospheric flows. *Acta Numer.*, **16**, 67–154.

848 Davies, T., M. J. P. Cullen, A. J. Malcolm, M. H. Mawson, A. Staniforth, A. White, and
849 N. Wood, 2005: A new dynamical core for the Met Office’s global and regional modelling
850 of the atmosphere. *Q. J. R. Meteorol. Soc.*, **131**, 1759–1782.

851 Davies, T., A. Staniforth, N. Wood, and J. Thuburn, 2003: Validity of anelastic and other
852 equation sets as inferred from normal-mode analysis. *Q. J. R. Meteorol. Soc.*, **129**, 2761–
853 2775.

854 Dukowicz, J. K., 2013: Evaluation of various approximations in ocean and atmospheric
855 modeling based on an exact treatment of gravity wave dispersion. *Mon. Wea. Rev.*, **141**,
856 4487–4506.

857 Durran, D. R., 1989: Improving the anelastic approximation. *J. Atmos. Sci.*, **46**, 1453–1461.

858 Durran, D. R., 2008: A physically motivated approach for filtering acoustic waves from the
859 equations governing compressible stratified flow. *J. Fluid. Mech.*, **601**, 365–379.

- 860 Durran, D. R. and P. N. Blossey, 2012: Implicit-explicit multistep methods for fast-wave-
861 slow-wave problems. *Mon. Wea. Rev.*, **140**, 1307–1325.
- 862 Falgout, R. D., J. E. Jones, and U. M. Yang, 2006: The design and implementation of
863 *hypre*, a library of parallel high performance preconditioners. *Numerical Solution of Partial*
864 *Differential Equations on Parallel Computers*, A. Bruaset and A. Tveito, Eds., Springer
865 Berlin Heidelberg, Lecture Notes in Computational Science and Engineering, Vol. 51,
866 267–294.
- 867 Gatti-Bono, C. and P. Colella, 2006: An anelastic allspeed projection method for gravita-
868 tionally stratified flows. *J. Comput. Phys.*, **216**, 589–615.
- 869 Giraldo, F. X., J. F. Kelly, and E. M. Costantinescu, 2013: Implicit-explicit formulations of
870 a three-dimensional nonhydrostatic unified model of the atmosphere (NUMA). *SIAM J.*
871 *Sci. Comput.*, **35**, B1162–B1194.
- 872 Gottlieb, S., C.-W. Shu, and E. Tadmor, 2001: Strong stability-preserving high-order time
873 discretization methods. *SIAM Rev.*, **43**, 89–112.
- 874 Haack, J., S. Jin, and J.-G. Liu, 2012: An all-speed asymptotic-preserving method for the
875 isentropic Euler and Navier-Stokes equations. *Commun. Comp. Phys.*, **12**, 955–980.
- 876 Hohenegger, C. and C. Schär, 2007: Predictability and error growth dynamics in cloud-
877 resolving models. *J. Atmos. Sci.*, **64**, 4467–4478.
- 878 Hornung, R. D., A. M. Wissink, and S. R. Kohn, 2006: Managing complex data and geometry
879 in parallel structured AMR applications. *Eng. Comp.*, **22**, 181–195.
- 880 Hortal, M., 2002: The development and testing of a new two-time-level semi-Lagrangian
881 scheme (SETTLS) in the ECMWF forecast model. *Q. J. R. Meteorol. Soc.*, **128**, 1671–
882 1687.

- 883 Janjic, Z. I., J. P. Gerrity, and S. Nickovic, 2001: An alternative approach to nonhydrostatic
884 modeling. *Mon. Wea. Rev.*, **129**, 1164–1178.
- 885 Jebens, S., O. Knoth, and R. Weiner, 2009: Explicit Two-Step Peer Methods for the Com-
886 pressible Euler Equations. *Mon. Wea. Rev.*, **137**, 2380–2392.
- 887 Jebens, S., O. Knoth, and R. Weiner, 2011: Partially implicit peer methods for the com-
888 pressible Euler equations. *J. Comput. Phys.*, **230**, 4955–4974.
- 889 Kadioglu, S. Y., R. Klein, and M. L. Minion, 2008: A fourth-order auxiliary variable pro-
890 jection method for zero-Mach number gas dynamics. *J. Comput. Phys.*, **227**, 2012–2043.
- 891 Kelly, J. F. and F. X. Giraldo, 2012: Continuous and discontinuous Galerkin methods for
892 a scalable three-dimensional nonhydrostatic atmospheric model: Limited-area mode. *J.*
893 *Comput. Phys.*, **231**, 7988–8008.
- 894 Klein, R., 2000: Asymptotic analyses for atmospheric flows and the construction of asymp-
895 totically adaptive numerical methods. *Z. Angew. Math. Mech.*, **80**, 765–777.
- 896 Klein, R., 2009: Asymptotics, structure, and integration of sound-proof atmospheric flow
897 equations. *Theor. Comp. Fluid Dyn.*, **23**, 161–195.
- 898 Klein, R., 2010: Scale-dependent models for atmospheric flows. *Annu. Rev. Fl. Mech.*, **42**,
899 249–274.
- 900 Klein, R., U. Achatz, D. Bresch, O. M. Knio, and P. Smolarkiewicz, 2010: Regime of validity
901 of soundproof atmospheric flow models. *J. Atmos. Sci.*, **67**, 3226–3237.
- 902 Klein, R., T. Benacchio, and W. P. O’Neill, 2013: Using the sound–proof limit for bal-
903 anced data initialization. *Proceedings of the ECMWF Seminar on Numerical Methods*,
904 *2-5 September, 2013*, Reading, UK, in press.

905 Klein, R., N. Botta, L. Hofmann, A. Meister, C. Munz, S. Roller, and T. Sonar, 2001:
906 Asymptotic adaptive methods for multiscale problems in fluid mechanics. *J. Eng. Math.*,
907 **39**, 261–343.

908 Klein, R. and O. Pauluis, 2011: Thermodynamic consistency of a pseudoincompressible
909 approximation for general equations of state. *J. Atmos. Sci.*, **69**, 961–968.

910 Konor, C. S., 2014: Design of a dynamical core based on the nonhydrostatic “unified system”
911 of equations. *Mon. Wea. Rev.*, **142**, 364–385.

912 Kwatra, N., J. Su, J. T. Grétarsson, and R. Fedkiw, 2009: A method for avoiding the acoustic
913 time step restriction in compressible flow. *J. Comput. Phys.*, **228**, 4146–4161.

914 LeVeque, R. J., 2002: *Finite Volume Methods for Hyperbolic Problems*. Cambridge University
915 Press, 580 pp.

916 Lipps, F. B. and R. S. Hemler, 1982: A scale analysis of deep moist convection and some
917 related numerical calculations. *J. Atmos. Sci.*, **39**, 2192–2210.

918 Munz, C.-D., S. Roller, R. Klein, and K. Geratz, 2003: The extension of incompressible flow
919 solvers to the weakly compressible regime. *Comput. Fluids*, **32**, 173–196.

920 Nonaka, A., A. S. Almgren, J. B. Bell, M. J. Lijewski, C. M. Malone, and M. Zingale, 2010:
921 MAESTRO: An adaptive low Mach number hydrodynamics algorithm for stellar flows.
922 *Astrophys. J. Suppl. S.*, **188**, 358.

923 Prusa, J. M. and W. J. Gutowski, 2011: Multi-scale waves in sound-proof global simulations
924 with EULAG. *Acta Geophys.*, **59**, 1135–1157.

925 Rabier, F., 2005: Overview of global data assimilation developments in numerical weather-
926 prediction centres. *Q. J. R. Meteorol. Soc.*, **131**, 3215–3233.

- 927 Reisner, J. M., A. Mousseau, A. A. Wyszogrodzki, and D. A. Knoll, 2005: An implicit-
928 itly balanced hurricane model with physics-based preconditioning. *Mon. Wea. Rev.*, **133**,
929 1003–1022.
- 930 Restelli, M. and F. X. Giraldo, 2009: A conservative discontinuous Galerkin semi-implicit
931 formulation for the Navier-Stokes equations in nonhydrostatic mesoscale modeling. *SIAM*
932 *J. Sci. Comput.*, **31**, 2231–2257.
- 933 Schneider, T., N. Botta, K. J. Geratz, and R. Klein, 1999: Extension of finite volume
934 compressible flow solvers to multi-dimensional, variable density zero Mach number flows.
935 *J. Comput. Phys.*, **155**, 248–286.
- 936 Skamarock, W. C. and J. B. Klemp, 1994: Efficiency and accuracy of the Klemp-Wilhelmson
937 time-splitting technique. *Mon. Wea. Rev.*, **122**, 2623–2630.
- 938 Skamarock, W. C. and J. B. Klemp, 2008: A time-split nonhydrostatic atmospheric model
939 for weather research and forecasting applications. *J. Comput. Phys.*, **227**, 3465–3485.
- 940 Smith, J. W. and P. R. Bannon, 2008: A comparison of compressible and anelastic models
941 of deep dry convection. *Mon. Wea. Rev.*, **136**, 4555–4571.
- 942 Smolarkiewicz, P. and P. Charbonneau, 2013: EULAG, a computational model for multiscale
943 flows: An MHD extension. *J. Comp. Phys.*, **236**, 608–623.
- 944 Smolarkiewicz, P., C. Kühnlein, and N. Wedi, 2014: A consistent framework for discrete
945 integrations of soundproof and compressible PDEs of atmospheric dynamics. *J. Comput.*
946 *Phys.*, **263**, 185–205.
- 947 Smolarkiewicz, P. K. and A. Dörnbrack, 2008: Conservative integrals of adiabatic Durran’s
948 equations. *Int. J. Numer. Meth. Fl.*, **56**, 1513–1519.
- 949 Straka, J. M., R. B. Wilhelmson, L. J. Wicker, J. R. Anderson, and K. K. Droegemeier,

950 1993: Numerical solutions of a non-linear density current: A benchmark solution and
951 comparisons. *Int. J. Numer. Meth. Fl.*, **17**, 1–22.

952 Szmelter, J. and P. K. Smolarkiewicz, 2011: An edge-based unstructured mesh framework
953 for atmospheric flows. *Comput. Fluids*, **46**, 455–460.

954 Vasil, G. M., D. Lecoanet, B. P. Brown, T. S. Wood, and E. G. Zweibel, 2013: Energy con-
955 servation and gravity waves in sound-proof treatments of stellar interiors. II. Lagrangian
956 constrained analysis. *Astrophys. J.*, **773**, 169.

957 Vater, S., 2013: A multigrid-based multiscale numerical scheme for shallow water flows
958 at low Froude number. Ph.D. thesis, Freie Universität Berlin, 179 pp., [Available at:
959 http://edocs.fu-berlin.de/diss/receive/FUDISS_thesis_000000093897].

960 Vater, S. and R. Klein, 2009: Stability of a cartesian grid projection method for zero Froude
961 number shallow water flows. *Numer. Math.*, **113**, 123–161.

962 Weller, H. and A. Shahrokhi, 2014: Curl-free pressure gradients over orography in a solution
963 of the fully compressible euler equations with long time-steps. *Mon. Wea. Rev.*, submitted.

964 Wong, M., W. C. Skamarock, P. H. Lauritzen, J. B. Klemp, and R. B. Stull, 2014: A com-
965 pressible nonhydrostatic cell-integrated semi-Lagrangian semi-implicit solver (CSLAM-
966 NH) with consistent and conservative transport. *Mon. Wea. Rev.*, **142**, 1669–1687.

967 Wood, N., et al., 2013: An inherently mass-conserving semi-implicit semi-Lagrangian dis-
968 cretization of the deep-atmosphere global non-hydrostatic equations. *Q. J. R. Meteorol.*
969 *Soc.*, in press, doi:10.1002/qj.2235.

970 Zängl, G., D. Reinert, P. Rípodas, and M. Baldauf, 2014: The ICON (ICOsahedral Nonhy-
971 drostatic) modelling framework of DWD and MPI-M: Description of the nonhydrostatic
972 dynamical core. *Q. J. R. Meteorol. Soc.*, in press, doi:10.1002/qj.2378.

⁹⁷³ Zingale, M., et al., 2002: Mapping initial hydrostatic models in Godunov codes. *Astrophys.*
⁹⁷⁴ *J. Suppl. S.*, **143**, 539–565.

List of Tables

975			
976	1	Model configurations used in the numerical scheme.	47
977	2	Rising bubble results: maximum temperature perturbation θ'_{\max} , attained	
978		height z_{\max} , and horizontal extension $x_{\max} - x_{\min}$ at final time $T = 1000$ s for	
979		FC, $\text{PI}_{\rho,p}^{\text{tc}}$, and $\text{PI}_{\rho,p}$ models. The values refer to the external contour at 0.25 K.	48
980	3	Rising bubble results: relative root-mean square error $E_{\text{rel}}^{\text{rms}}$ and maximum	
981		error $E_{\text{rel}}^{\text{max}}$ on potential temperature perturbation profile θ' and maximum	
982		error $E_{\text{rel}}^{\text{max}}$ on the maximum perturbation amplitude θ'_{\max} for the $\text{PI}_{\rho,p}^{\text{tc}}$ and	
983		$\text{PI}_{\rho,p}$ cuts at $z = 7500$ m with respect to the FC cut as in figure 5.	49
984	4	Density current results: maximum temperature perturbation θ'_{\max} and front	
985		position x_{\max} at final time $T = 900$ s. x_{\max} is the rightmost intersection of	
986		the 1 K contour with the bottom boundary.	50
987	5	Density current results: relative root-mean square error $E_{\text{rel}}^{\text{rms}}$ and maximum	
988		error $E_{\text{rel}}^{\text{max}}$ on potential temperature perturbation profile θ' and maximum	
989		error $E_{\text{rel}}^{\text{max}}$ on the maximum perturbation amplitude θ'_{\max} for the $\text{PI}_{\rho,p}^{\text{tc}}$ and	
990		$\text{PI}_{\rho,p}$ cuts at $z = 1200$ m with respect to the FC cut as in figure 9.	51
991	6	Inertia-gravity wave results: maxima and minima of horizontal velocity u ,	
992		vertical velocity w , potential temperature θ and Exner pressure $\pi = T\theta^{-1}$	
993		perturbations at final time $T = 3000$ s in the present study and Restelli and	
994		Giraldo (2009) (denoted with REF).	52
995	7	Inertia-gravity wave results: relative root-mean square error $E_{\text{rel}}^{\text{rms}}$ and maxi-	
996		imum error $E_{\text{rel}}^{\text{max}}$ on potential temperature perturbation profile θ' for the $\text{PI}_{\rho,p}^{\text{tc}}$	
997		and $\text{PI}_{\rho,p}$ cuts at $z = 5000$ m with respect to the FC cut as in figure 11.	53
998	8	Inertia-gravity wave results: conservation errors for density, horizontal mo-	
999		mentum density, P and total energy density (see text for definitions) in the	
1000		present study and in Restelli and Giraldo (2009), denoted with REF.	54

Model name	Abbreviation	(α, β)
Fully-compressible	FC	$(1, 0)$
Thermodynamically Consistent Pseudo-incompressible	$\text{PI}_{\rho,p}^{\text{tc}}$	$(0, 1)$
Non-thermodynamically Consistent Pseudo-incompressible	$\text{PI}_{\rho,p}$	$(0, 0)$

TABLE 1. Model configurations used in the numerical scheme.

	θ'_{\max}	z_{\max}	$x_{\max} - x_{\min}$
FC	1.64 K	8183 m	6637 m
PI $_{\rho,p}^{\text{tc}}$	1.64 K	8187 m	6648 m
PI $_{\rho,p}$	1.65 K	8469 m	6278 m

TABLE 2. Rising bubble results: maximum temperature perturbation θ'_{\max} , attained height z_{\max} , and horizontal extension $x_{\max} - x_{\min}$ at final time $T = 1000$ s for FC, PI $_{\rho,p}^{\text{tc}}$, and PI $_{\rho,p}$ models. The values refer to the external contour at 0.25 K.

	$E_{\text{rel}}^{\text{rms}}(\theta')$	$E_{\text{rel}}^{\text{max}}(\theta')$	$E_{\text{rel}}^{\text{max}}(\theta'_{\text{max}})$
PI $_{\rho,p}^{\text{tc}}$ -FC	0.017	0.018	1.07E-03
PI $_{\rho,p}$ -FC	0.57	0.57	3.61E-02

TABLE 3. Rising bubble results: relative root-mean square error $E_{\text{rel}}^{\text{rms}}$ and maximum error $E_{\text{rel}}^{\text{max}}$ on potential temperature perturbation profile θ' and maximum error $E_{\text{rel}}^{\text{max}}$ on the maximum perturbation amplitude θ'_{max} for the PI $_{\rho,p}^{\text{tc}}$ and PI $_{\rho,p}$ cuts at $z = 7500$ m with respect to the FC cut as in figure 5.

	θ'_{\max}	x_{\max}
FC	-10.14 K	15476 m
PI $_{\rho,p}^{\text{tc}}$	-10.17 K	15456 m
PI $_{\rho,p}$	-9.96 K	15676 m

TABLE 4. Density current results: maximum temperature perturbation θ'_{\max} and front position x_{\max} at final time $T = 900$ s. x_{\max} is the rightmost intersection of the 1 K contour with the bottom boundary.

	$E_{\text{rel}}^{\text{rms}}(\theta')$	$E_{\text{rel}}^{\text{max}}(\theta')$	$E_{\text{rel}}^{\text{max}}(\theta'_{\text{max}})$
PI $_{\rho,p}^{\text{tc}}$ -FC	0.046	0.090	1.93E-03
PI $_{\rho,p}$ -FC	0.441	0.584	0.026

TABLE 5. Density current results: relative root-mean square error $E_{\text{rel}}^{\text{rms}}$ and maximum error $E_{\text{rel}}^{\text{max}}$ on potential temperature perturbation profile θ' and maximum error $E_{\text{rel}}^{\text{max}}$ on the maximum perturbation amplitude θ'_{max} for the PI $_{\rho,p}^{\text{tc}}$ and PI $_{\rho,p}$ cuts at $z = 1200$ m with respect to the FC cut as in figure 9.

	u'_{\max}	u'_{\min}	w'_{\max}	w'_{\min}	θ'_{\max}	θ'_{\min}	π'_{\max}	π'_{\min}
FC	1.054E-2	-1.060E-2	2.739E-3	-2.262E-3	2.808E-3	-1.526E-3	7.75E-7	-5.27E-7
PI $_{\rho,p}^{\text{tc}}$	1.063E-2	-1.063E-2	2.645E-3	-2.424E-3	2.808E-3	-1.526E-3	1.18E-5	-6.56E-7
PI $_{\rho,p}$	1.365E-2	-1.362E-2	2.764E-3	-2.471E-3	2.930E-3	-1.709E-3	1.21E-5	-5.36E-7
REF	1.064E-2	-1.061E-2	2.877E-3	-2.400E-3	2.808E-3	-1.511E-3	9.11E-7	-7.13E-7

TABLE 6. Inertia-gravity wave results: maxima and minima of horizontal velocity u , vertical velocity w , potential temperature θ and Exner pressure $\pi = T\theta^{-1}$ perturbations at final time $T = 3000$ s in the present study and Restelli and Giraldo (2009) (denoted with REF).

	$E_{\text{rel}}^{\text{rms}}(\theta')$	$E_{\text{rel}}^{\text{max}}(\theta')$
PI $_{\rho,p}^{\text{tc}}$ -FC	0.039	0.055
PI $_{\rho,p}$ -FC	0.132	0.16

TABLE 7. Inertia-gravity wave results: relative root-mean square error $E_{\text{rel}}^{\text{rms}}$ and maximum error $E_{\text{rel}}^{\text{max}}$ on potential temperature perturbation profile θ' for the PI $_{\rho,p}^{\text{tc}}$ and PI $_{\rho,p}$ cuts at $z = 5000$ m with respect to the FC cut as in figure 11.

	C_ρ	$C_{\rho u}$	C_P	$C_{\rho E}$
FC	1.15E-09	8.05E-11	5.68E-09	1.98E-09
PI $_{\rho,p}^{\text{tc}}$	6.77E-10	9.66E-10	\	3.99E-09
PI $_{\rho,p}$	8.90E-10	8.55E-10	\	4.21E-09
REF	1.67E-08	2.60E-07	\	1.64E-08

TABLE 8. Inertia-gravity wave results: conservation errors for density, horizontal momentum density, P and total energy density (see text for definitions) in the present study and in Restelli and Giraldo (2009), denoted with REF.

1001 List of Figures

- 1002 1 Computational grid for the numerical scheme. Solid lines define cells; dashed
1003 lines define dual cells, used for the second correction. Dots, squares and
1004 crosses denote cell centers, nodes, and interface centers, respectively. 58
- 1005 2 Smoothed rotating vortex results: density (left) and pressure (right). The
1006 upper row shows initial data. The lower row shows computed values at
1007 $T = 1$ s with the FC model. Contours are plotted every 0.025 kg m^{-3} in
1008 $[0.525, 0.975] \text{ kg m}^{-3}$ for density, every 0.025 Pa in the interval $[-0.025, -0.3] \text{ Pa}$
1009 for pressure. The domain is discretized with 192 cells in each direction with
1010 $\text{CFL} = 0.45$. 59
- 1011 3 Smoothed rotating vortex results: density (left), momentum norm (middle)
1012 and pressure (right) convergence story. Errors are shown in the maximum
1013 norm of computed solutions at $T = 1$ s on grids with 64^2 , 128^2 , 256^2 , and
1014 512^2 cells with respect to computed solutions on a reference grid with 1024^2
1015 cells. The numbers inside the graphs are the experimental rates of conver-
1016 gence between subsequent grid refinements. The dashed-dotted line represents
1017 quadratic slope. 60
- 1018 4 Rising bubble results. Panels show potential temperature initial data (upper
1019 left) and computed value at $T = 1000$ s with the FC (upper right), $\text{PI}_{\rho,p}^{\text{tc}}$
1020 (lower left) and $\text{PI}_{\rho,p}$ models (lower right). Contours are plotted every 0.25 K
1021 starting at 300.25 K . 61
- 1022 5 Rising bubble results: potential temperature perturbation at final time $T =$
1023 1000 s. The left panel shows a horizontal cut of the final θ' at height $z =$
1024 7500 m of the FC (solid line), $\text{PI}_{\rho,p}^{\text{tc}}$ (cross-marked line) and $\text{PI}_{\rho,p}$ (dashed-
1025 dotted line). The right panel shows the difference from the FC cut of the
1026 $\text{PI}_{\rho,p}^{\text{tc}}$ cut(solid line) and the $\text{PI}_{\rho,p}$ cut(dashed-dotted line). 62

- 1027 6 Rising bubble results, nodal pressure time increment δp . The upper left panel
1028 shows contours of δp every .6 Pa starting at -3 Pa, time step 14 ($t = 26.6$ s),
1029 FC model. The right panels shows the value of δp over the first 350 s measured
1030 at $(x, z) = (-7.5, 5)$ km for FC (solid line) and $\text{PI}_{\rho,p}$ (dashed line) configu-
1031 rations. In the upper right panel the time step is constant and $\Delta t = 1.9$ s.
1032 The lower left panel displays the value of δp over the first 350 s measured at
1033 the same location. Blended runs at constant $\Delta t = 1.9$ s with $S_1 = 10$ initial
1034 pseudo-incompressible steps and $S_2 = 20$ (dashed-dotted line) and $S_2 = 40$
1035 (thick solid line) transitional steps are compared with the fully-compressible
1036 run, $S_1 = S_2 = 0$ (thin solid line). The dashed-dotted line in the lower right
1037 panel refers to a blended run with $S_1 = 0$, $S_2 = 3$. In the lower right panel
1038 the time step is determined by $\text{CFL} = 0.5$ (initial $\Delta t \approx 21.69$ s) and the data
1039 for the first time step is removed. 63
- 1040 7 Rising bubble results: Mach number M at time step 56 ($T \approx 21.66$ s for
1041 $\Delta t = 0.38$ s); left: FC model, $S_1 = S_2 = 0$; middle: $\text{PI}_{\rho,p}$ model; right: $\text{PI}_{\rho,p}$ -
1042 then-FC model, $S_1 = 10$, $S_2 = 40$. Contours are plotted every 10^{-4} in the
1043 range $[0.0001, 0.002]$. 64
- 1044 8 Density current results: potential temperature perturbation. Panels shows
1045 initial data (upper left), FC results at $t = 300$ s (upper right), $t = 600$ s
1046 (lower left) and at $t = 900$ s (lower right). Contours are plotted every 1 K
1047 from -16.5 K to -0.5 K. 65
- 1048 9 Density current results: potential temperature perturbation at final time $T =$
1049 900 s. The left panel shows a horizontal cut at height $z = 1200$ m. The right
1050 panel shows the difference from the FC profile of the $\text{PI}_{\rho,p}^{\text{tc}}$ profile (solid line)
1051 and of the $\text{PI}_{\rho,p}$ profile(dashed line). 66

- 1052 10 Inertia-gravity wave results: potential temperature perturbation. The left
1053 panel shows initial data, contours every 10^{-3} K; the right panel shows FC
1054 result at $T = 3000$ s, contours every $5 \cdot 10^{-4}$ K in the range $[-0.0015, 0.003]$ K.
1055 Thin lines denote negative contours. 67
- 1056 11 Inertia-gravity wave results: potential temperature perturbation at final time.
1057 The left panel shows a horizontal cut at height $z = 5000$ m for the FC model
1058 (solid line), the $\text{PI}_{\rho,p}^{\text{tc}}$ model (stars), and the $\text{PI}_{\rho,p}$ model (dashed-dotted line).
1059 The region of the leftmost crest is magnified to highlight the higher phase
1060 speed of the $\text{PI}_{\rho,p}$ model. The right panel shows the difference from the FC
1061 cut for the $\text{PI}_{\rho,p}^{\text{tc}}$ cut (solid line) and the $\text{PI}_{\rho,p}$ cut (dashed line). 68

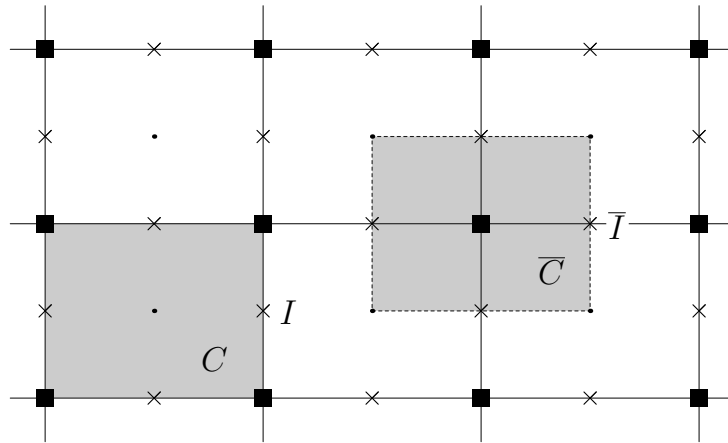


FIG. 1. Computational grid for the numerical scheme. Solid lines define cells; dashed lines define dual cells, used for the second correction. Dots, squares and crosses denote cell centers, nodes, and interface centers, respectively.

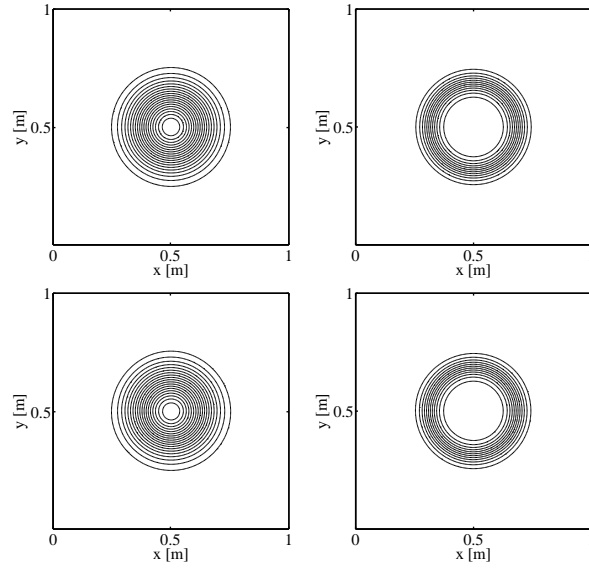


FIG. 2. Smoothed rotating vortex results: density (left) and pressure (right). The upper row shows initial data. The lower row shows computed values at $T = 1$ s with the FC model. Contours are plotted every 0.025 kg m^{-3} in $[0.525, 0.975] \text{ kg m}^{-3}$ for density, every 0.025 Pa in the interval $[-0.025, -0.3] \text{ Pa}$ for pressure. The domain is discretized with 192 cells in each direction with $\text{CFL} = 0.45$.

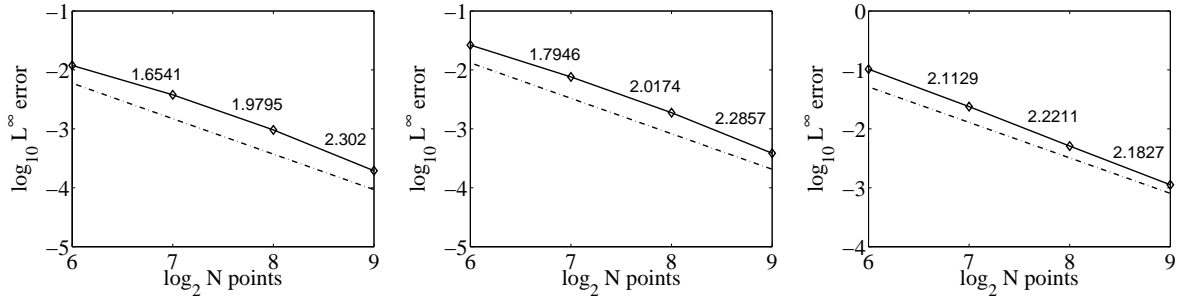


FIG. 3. Smoothed rotating vortex results: density (left), momentum norm (middle) and pressure (right) convergence story. Errors are shown in the maximum norm of computed solutions at $T = 1$ s on grids with 64^2 , 128^2 , 256^2 , and 512^2 cells with respect to computed solutions on a reference grid with 1024^2 cells. The numbers inside the graphs are the experimental rates of convergence between subsequent grid refinements. The dashed-dotted line represents quadratic slope.

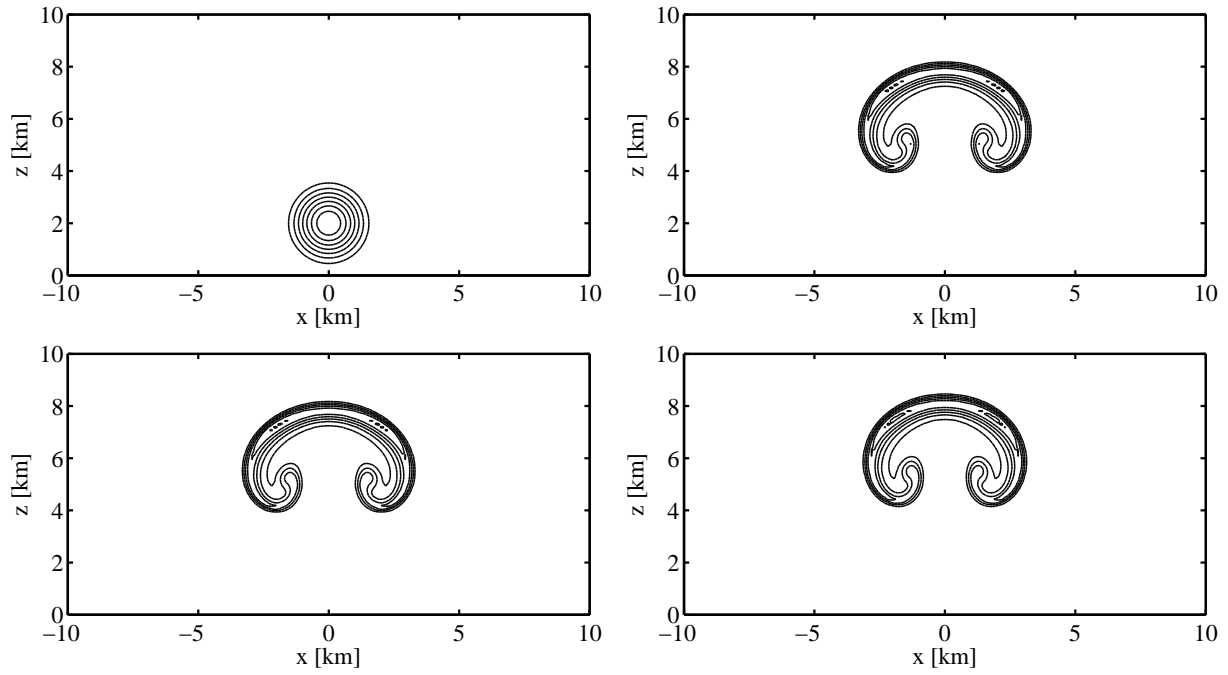


FIG. 4. Rising bubble results. Panels show potential temperature initial data (upper left) and computed value at $T = 1000$ s with the FC (upper right), $\text{PI}_{\rho,p}^{\text{tc}}$ (lower left) and $\text{PI}_{\rho,p}$ models (lower right). Contours are plotted every 0.25 K starting at 300.25 K.

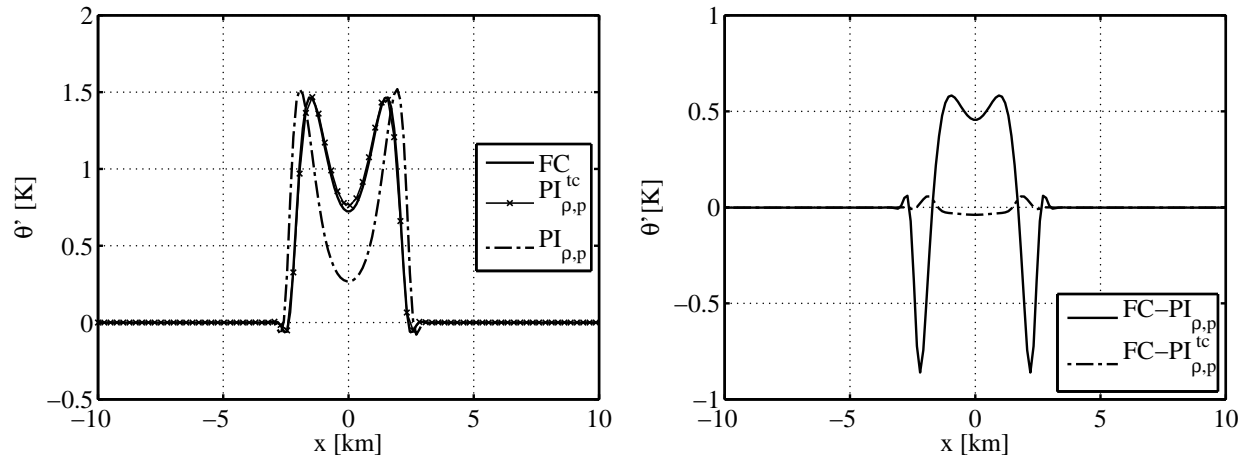


FIG. 5. Rising bubble results: potential temperature perturbation at final time $T = 1000$ s. The left panel shows a horizontal cut of the final θ' at height $z = 7500$ m of the FC (solid line), $\text{PI}_{\rho,p}^{\text{tc}}$ (cross-marked line) and $\text{PI}_{\rho,p}$ (dashed-dotted line). The right panel shows the difference from the FC cut of the $\text{PI}_{\rho,p}^{\text{tc}}$ cut (solid line) and the $\text{PI}_{\rho,p}$ cut (dashed-dotted line).

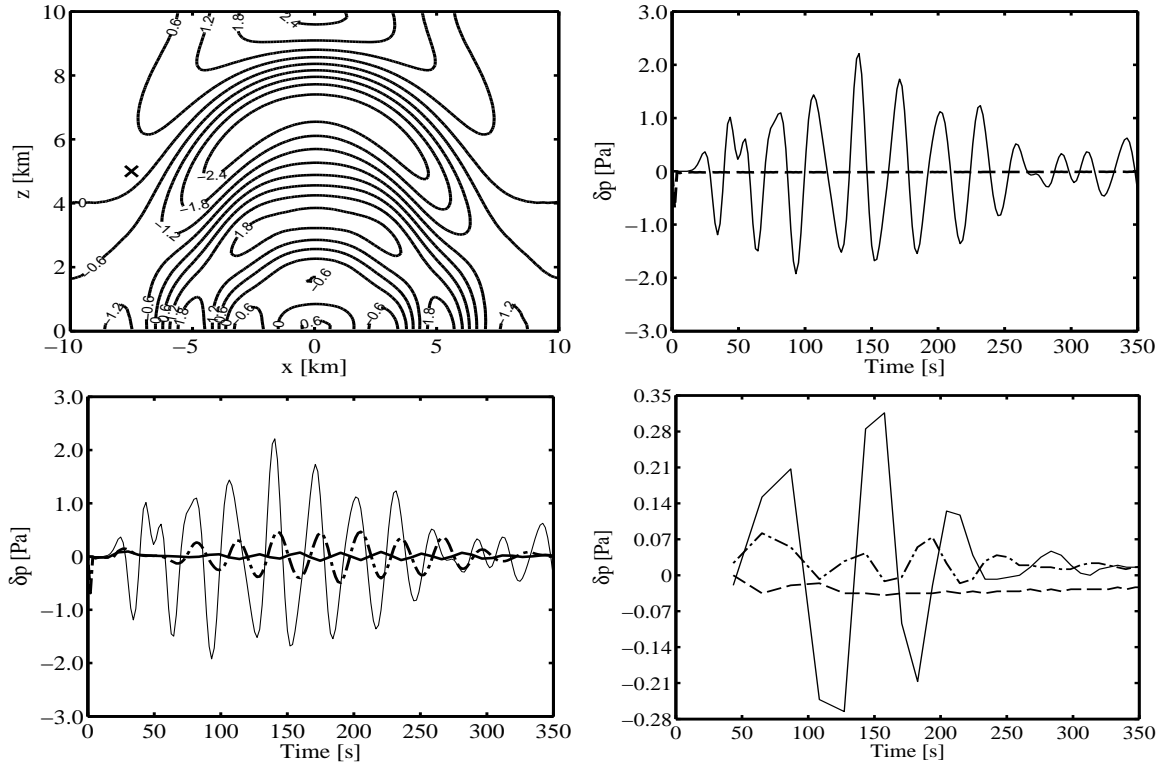


FIG. 6. Rising bubble results, nodal pressure time increment δp . The upper left panel shows contours of δp every .6 Pa starting at -3 Pa, time step 14 ($t = 26.6$ s), FC model. The right panels shows the value of δp over the first 350 s measured at $(x, z) = (-7.5, 5)$ km for FC (solid line) and $PI_{\rho,p}$ (dashed line) configurations. In the upper right panel the time step is constant and $\Delta t = 1.9$ s. The lower left panel displays the value of δp over the first 350 s measured at the same location. Blended runs at constant $\Delta t = 1.9$ s with $S_1 = 10$ initial pseudo-incompressible steps and $S_2 = 20$ (dashed-dotted line) and $S_2 = 40$ (thick solid line) transitional steps are compared with the fully-compressible run, $S_1 = S_2 = 0$ (thin solid line). The dashed-dotted line in the lower right panel refers to a blended run with $S_1 = 0$, $S_2 = 3$. In the lower right panel the time step is determined by $CFL = 0.5$ (initial $\Delta t \approx 21.69$ s) and the data for the first time step is removed.

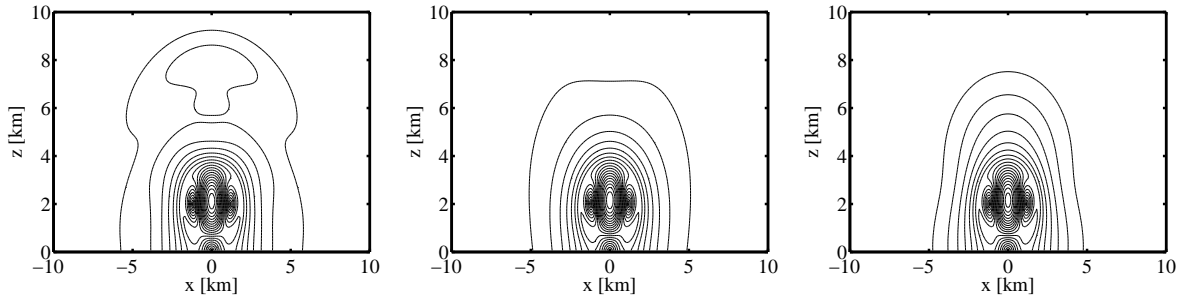


FIG. 7. Rising bubble results: Mach number M at time step 56 ($T \approx 21.66$ s for $\Delta t = 0.38$ s); left: FC model, $S_1 = S_2 = 0$; middle: $\text{PI}_{\rho,p}$ model; right: $\text{PI}_{\rho,p}$ -then-FC model, $S_1 = 10$, $S_2 = 40$. Contours are plotted every 10^{-4} in the range $[0.0001, 0.002]$.

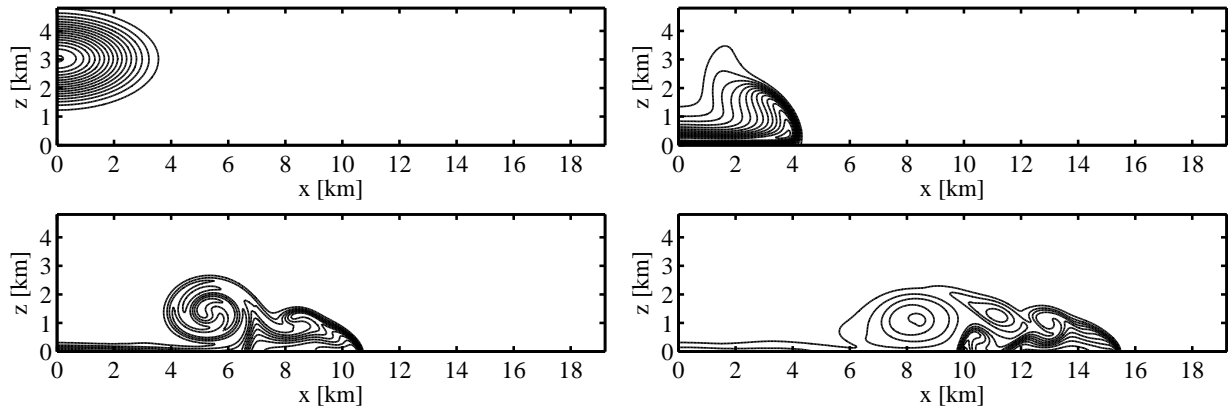


FIG. 8. Density current results: potential temperature perturbation. Panels shows initial data (upper left), FC results at $t = 300$ s (upper right), $t = 600$ s (lower left) and at $t = 900$ s (lower right). Contours are plotted every 1 K from -16.5 K to -0.5 K.

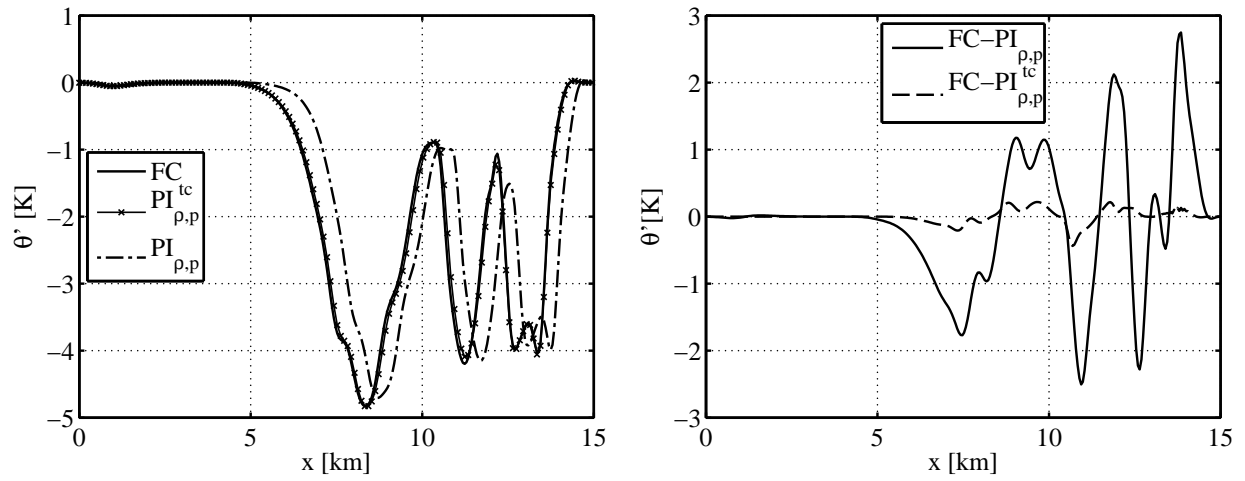


FIG. 9. Density current results: potential temperature perturbation at final time $T = 900$ s. The left panel shows a horizontal cut at height $z = 1200$ m. The right panel shows the difference from the FC profile of the $PI_{\rho,p}^{tc}$ profile (solid line) and of the $PI_{\rho,p}$ profile (dashed line).

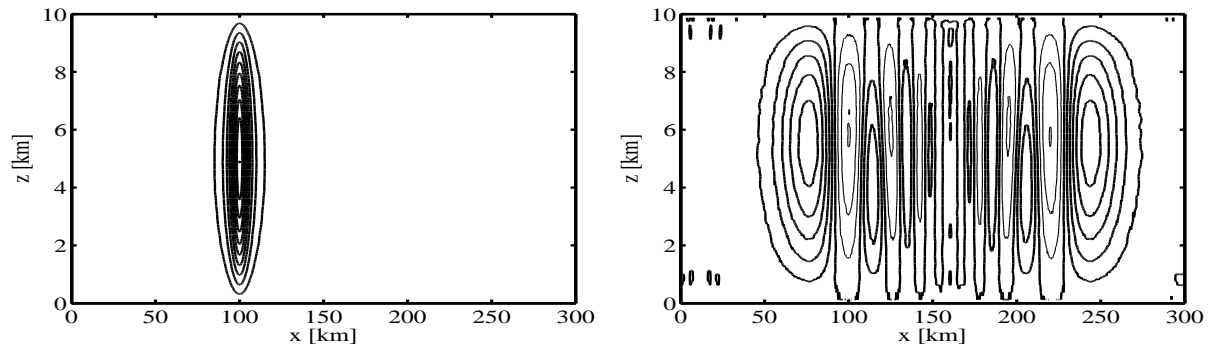


FIG. 10. Inertia-gravity wave results: potential temperature perturbation. The left panel shows initial data, contours every 10^{-3} K; the right panel shows FC result at $T = 3000$ s, contours every $5 \cdot 10^{-4}$ K in the range $[-0.0015, 0.003]$ K. Thin lines denote negative contours.

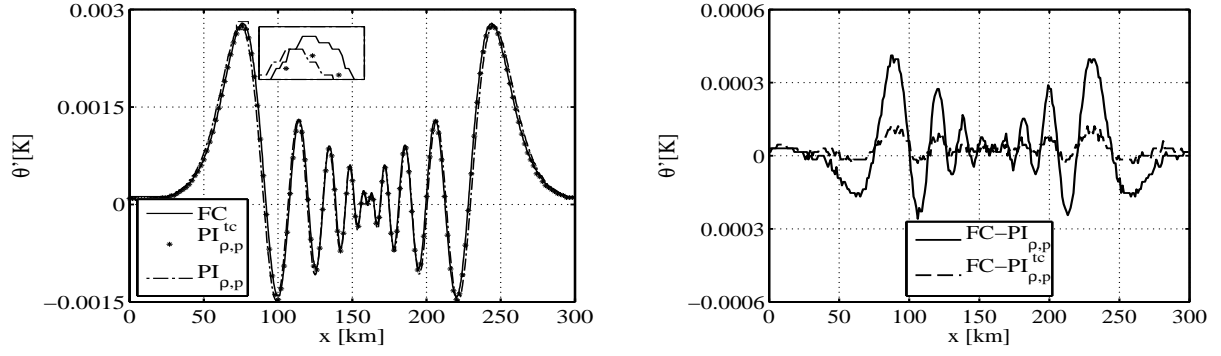


FIG. 11. Inertia-gravity wave results: potential temperature perturbation at final time. The left panel shows a horizontal cut at height $z = 5000$ m for the FC model (solid line), the $\text{PI}_{\rho,p}^{\text{tc}}$ model (stars), and the $\text{PI}_{\rho,p}$ model (dashed-dotted line). The region of the leftmost crest is magnified to highlight the higher phase speed of the $\text{PI}_{\rho,p}$ model. The right panel shows the difference from the FC cut for the $\text{PI}_{\rho,p}^{\text{tc}}$ cut (solid line) and the $\text{PI}_{\rho,p}$ cut (dashed line).